Seasonal variation of local atmospheric circulations and boundary layer structure in the Beijing-Tianjin-Hebei region and implications for air quality

Yucong Miao[1], Xiao-Ming Hu[2, 3], Shuhua Liu[1], Tingting Qian[4], Ming Xue[3], Yijia Zheng[1], Shu Wang[1]

[1]Department of Atmospheric and Oceanic Sciences, School of Physics, Peking University, Beijing 100871, China

[2]Key Laboratory of Meteorological Disaster of Ministry of Education，Nanjing University of Information Science and Technology, Nanjing 210044, China

[3]Center for Analysis and Prediction of Storms, and School of Meteorology, University of Oklahoma, Norman, OK 73072, USA

[4]State Key Laboratory of Severe Weather, Chinese Academy of Meteorological Sciences, Beijing 100081, China

Submitted to *Journal of Advances in Modeling Earth Systems*

1st submission 3/24/2015; revised on 9/28/2015

Corresponding author address:

Dr. Xiao-Ming Hu

Center for Analysis and Prediction of Storms, and School of Meteorology

University of Oklahoma

Norman, Oklahoma, 73072, USA

Email: xhu@ou.edu (X.-M. Hu)

Phone: (405)325- 5571

Key points

1. Seasonal variation of BL processes in the BTH region are examined using idealized simulations

2. Seasonal variation of daytime BL height over most of BTH is spring > summer > fall > winter

3. Seasonal variation of BL processes/structure modulates seasonal variation of air pollution

Abstract

The Beijing-Tianjin-Hebei (BTH) region experiences frequent heavy haze pollution in fall and winter. Pollution was often exacerbated by unfavorable atmospheric boundary layer (BL) conditions. The topography in this region impacts the BL processes in complex ways. Such impacts and implications on air quality are not yet clearly understood. The BL processes in all four seasons in BTH are thus investigated in this study using idealized simulations with the WRF/Chem model. Results suggest that seasonal variation of thermal conditions and synoptic patterns significantly modulates BL processes. In fall, with a relatively weak northwesterly synoptic forcing, thermal contrast between the mountains and the plain leads to a prominent mountain-plain breeze circulation (MPC). In the afternoon, the downward branch of the MPC, in addition to northwesterly warm advection, suppresses BL development over the western side of BTH. In the eastern coastal area, a sea-breeze circulation develops late in the morning and intensifies during the afternoon. In summer, southeasterly BL winds allow the see-breeze front to penetrate farther inland (~150 km from the coast), and the MPC is less prominent. In spring and winter, with strong northwesterly synoptic winds, the sea-breeze circulation is confined in the coastal area, and the MPC is suppressed. The BL height is low in winter due to strong near-surface stability, while BL heights are large in spring due to strong mechanical forcing. The relatively low BL height in fall and winter may have exacerbated the air pollution, thus contributing to the frequent severe haze events in the BTH region.

Index Terms: 0345 Pollution: urban and regional; 3307 Boundary layer processes

Keywords: Seasonal climate, air pollution, local atmospheric circulations, boundary layer structure, WRF, Beijing-Tianjin-Hebei

1. Introduction

The Beijing-Tianjin-Hebei (BTH) region, part of the North China Plain (NCP), is located along the northeastern coast of mainland China and includes the Beijing municipality, Tianjin municipality, and Hebei province (Figure 1). The BTH region covers an area of 216,000 square km (about 2.3% of Chinese territory), and has a population exceeding 100 million. Due to the rapid industrialization and urbanization of the past few decades, the BTH region has become one of the most economically-developed regions in China, contributing more than 10% of the total Chinese gross domestic product (GDP) in 2010 [NBSC, 2011]. The rapid and tremendous economic development has resulted in frequent heavy air pollution in this region [Chan and Yao, 2008; Chen et al., 2013; He et al., 2001; Ji et al., 2014; Liu et al., 2013; Quan, et al., 2014; Sun et al., 2006; Tao et al, 2012; Xu et al., 2011; Zhang et al., 2013]; the BTH region is regarded as one of the most heavily polluted areas in the world [van Donkelaar et al., 2010; Huang et al., 2014].

Great efforts have been devoted to investigating air pollution issues in the BTH region. In addition to high emissions, meteorological factors have been found to play an important role in exacerbating air pollution in this region [Xu et al., 2011; Wang et al., 2014b; Liu et al., 2013; Hu et al., 2014; Sun et al., 2006; Qu et al., 2015; Zhang et al., 2015a]. Detailed statistical analysis conducted in Xu et al. [2011] and Zhang et al. [2015a] showed that the concentration of CO, SO_2 and NO_2 is reversely correlated with surface wind speed and O_3 is positively correlated with temperature in BTH. High aerosol levels in the BTH region were often associated with low wind speed and high relative humidity near the surface [Sun et al. 2006; Wu et al., 2008; An et al., 2007]. Southerly winds were more likely to lead to air pollution episodes in BTH [Fu et al., 2014, Zhao et al., 2009]. Partially due to the limited observations from the atmospheric boundary layer (BL), these previous studies have focused on the impact of surface meteorological variables on ambient air quality, and were not able to reveal the important role of BL processes/structure in dispersion of pollutants. Some recent studies have suggested that atmospheric BL conditions may play a more important role in determining pollutant concentrations in the BTH region [Quan et al., 2013; Hu et al., 2014; Sun et al., 2013; Liu et al., 2013; Wang et al., 2014b; Tie et al., 2014]. Low BL height (BLH) was found to be partially responsible for several air pollution episodes in the region [Quan et al., 2013; Liu et al., 2013; Wang et al., 2014a and 2014b]. Most of these studies, however, were limited to severe pollution cases [Liu et al., 2013; Wang et al., 2014b; Hu et al., 2014; Quan et al., 2013; Sun et al., 2013; Tie et al., 2014], and none investigated the role of seasonal variation of BL processes/structure on pollution levels in the BTH region.

Many previous studies have suggested a seasonal variation of frequency of air pollution events in the BTH region, with most of the ozone pollution events occurring in summer and most of the $PM_{2.5}$ dominated haze pollution events occurring in fall and winter [Fu et al., 2014; He et al., 2001; He et al., 2006; Liu et al., 2013; Quan et al., 2014; Ji et al., 2014; Wang et al., 2014b; Huang et al., 2014; Gao et al., 2015; Tie et al., 2014; Zhang et al., 2015a; Wang et al., 2011; San Martini et al., 2015]. In terms of coarse particles, a majority of the severe events were found to be associated with dust storms, which occurred most frequently in spring [Shao and Dong, 2006; Tian et al., 2014; Wang et al., 2005; Kurosaki and Mikami, 2003]. The causes for the seasonal variation of air pollution in BTH is, however, not clearly understood [Fu et al., 2014; He et al., 2001; Zhang et al., 2015a; Zhang et al., 2013]. It is speculated to be related to seasonal variation of emissions [Zhang et al., 2013; He et al., 2006] and near-surface meteorological conditions [Zhang et al., 2015a; Xu et al., 2011]. None of the previous studies attempted to attribute the causes for the seasonal variation of air pollution in this region to the seasonal variation of BL structure. One objective of the present study is to investigate the prominent seasonal variation of BL structure in the BTH region, which will be demonstrated in this study to play a critical role in modulating the seasonal variation of air pollution in BTH.

The topography in the BTH region impacts the BL processes and structure in complex ways [Xu et al., 2011; Sun et al., 2013; Liu et al., 2009b; Hu et al., 2014; Chen et al., 2009; Chan and Yao, 2008; Miao et al., 2015a; Wang et al., 2010]. With the Taihang Mountains to the west, the Yan Mountains to the north, and the Bohai Sea bordered to the east (Figure 1a), thermally induced local atmospheric circulations, such as the sea-breeze circulation and mountain-plain breeze circulation (MPC), develop frequently in the BTH region under favorable synoptic conditions [Chen et al., 2009; Sun et al., 2013; Liu et al., 2009b; Hu et al., 2014; Miao et al., 2015a].

The sea-breeze circulation is induced by thermal contrast between the land and sea, and influence the transport and distribution of pollutants over coastal regions [Miller et al., 2003]. The sea-breeze circulation has been investigated around the world in terms of its formation mechanism [Tijm et al., 1999; Reible et al., 1993; Qian et al., 2009], structure [Buckley and Kurzeja, 1997; Wood et al., 1999; Puygrenier et al., 2005], and its impact on air quality [Lo et al., 2006; Lu and Turco et al., 1994; Wu et al., 2013; Liu and Chan, 2002]. A few case studies have investigated the sea-breeze circulation in the BTH region [Sun et al., 2013; Liu et al., 2009; Miao et al., 2015a]. Liu et al. [2009b] and Miao et al. [2015a] reported that the sea-breeze in the BTH region can penetrate as far inland as the Langfang area (~100 km inland from the coast) on a clear summer day. Sun et al. [2013] demonstrated that the diurnal variation of sea-breeze circulation trapped the pollutants in the BTH region, resulting in serious pollution on 1-16 August 2009. The aforementioned studies were carried out for specific cases; none of them investigated the seasonal variation of sea-breeze circulation characteristics (e.g., extent of inland penetration) and the impacts of this seasonal variation on the BL structure in the BTH region.

In the presence of strong solar radiation, the near-surface air temperature over mountainous terrain during the daytime is normally higher than the air temperature at the same height over the adjacent plain [Banta and Cotton, 1981]. As a result, upslope winds develop near the mountainside surface; a return flow simultaneously develops aloft over the adjacent plain. At night, the thermal gradient (and the resultant circulation) are reversed. This thermally driven phenomenon is termed the mountain-plain breeze circulation (MPC). The MPC has been found to influence BL structure and air quality over various mountain-plain/valley regions, including the Freiburg area in Germany [Baumbach and Vogt, 1999], the Lower Fraser Valley in Canada [De Wekker 2008; Reuten et al., 2005], and the Inn Valley in Austria [Gohm et al., 2009]. It has recently been found that the BL structure and air quality in the BTH region may be affected by the MPC [Hu et al., 2014; Chen et al., 2009; Miao et al., 2015b]. Hu et al. [2014] reported that the MPC suppressed BL development in the NCP (where BTH is located) and exacerbated air pollution in an ozone episode. Chen et al. [2009] observed an elevated pollution layer above the BL over Beijing on 18 August 2007, which was attributed to vertical transport from the BL by the upward branch of the MPC. Miao et al. [2015b] reported that an elevated pollution layer induced by MPC may have served as a reservoir (and later contributed to a pollution event) in BTH on 23-24 September 2011. These previous studies focused on the effects of the MPC on BL structure and air quality in certain pollution episodes. The seasonal variation of MPC and its impacts on seasonal variation of air pollution in BTH, however, still remain unclear.

As a necessary first step to reveal the complicated causes for the seasonal variation of air pollution in BTH [Zhang et al., 2015a; Zhao et al. 2009; Yamaji, et al., 2006; Vecchi et al., 2001], the present study investigates the seasonal variation of local atmospheric circulations and BL structure in BTH and its impacts on air quality using idealized simulations with the Weather Research and Forecasting model with Chemistry (WRF-Chem) [Grell et al., 2005]. The remainder of this paper is organized as follows. Design of numerical experiments and observational data are described in section 2. The seasonal variations of BL processes/structure, as well as their implications for air quality in BTH, are examined in section 3. Finally, the findings of this study are summarized in section 4.

2. Methods

2.1 Design of numerical experiments

To investigate the seasonal characteristics of the BL processes in the BTH region and their impact on air quality, the WRF-Chem model (version 3.6) is used to conduct four idealized numerical experiments: one corresponding to each of the four seasons, i.e., winter (December, January, and February), spring (March, April, and May), summer (June, July, and August) and fall (September, October, and November). Since both meteorological and chemical processes modulate concentration of chemical species simultaneously, the first-order impact of meteorological processes on concentrations of particular species can be hardly isolated/identified with the full chemistry simulation. Thus, the WRF-Chem tracer (i.e. SO_2) simulations are conducted with the emission (Figure 1b) composed by Zhang et al. [2009] in this study, to demonstrate the first-order impact of BL processes on air quality in the BTH region. The boundary condition of SO_2 in the outermost domain is set as clean state, and the initial condition of SO_2 of each simulation is extracted from another 24-hour WRF-Chem tracer simulation initialized with the clean state. The lifetime of tropospheric SO_2 with respect to gas-phase oxidation is typically a few days [Eisinger and Burrows, 1998; Fiedler et al., 2009]. It may be not as ideal as other species with longer lifetimes (e.g., CO) to be treated as a strictly passive tracer, SO_2, however, can be treated as a "nearly" passive tracer when investigating its regional transport and accumulation [Fiedler et al., 2009]

Three one-way nested domains with horizontal grid spacings of 27, 9 and 3 km (Figure 1a) and the MODIS 2010 land use data (Figure 1c) are used in the WRF-Chem simulations. Each domain has 48 vertical layers extending from the surface to the 100 hPa level, with 21 layers between the surface and 2 km above ground level (AGL) to better resolve BL processes and structures. Since BL schemes plays a critical role in simulating BL processes/structure [Hu et al., 2010], four commonly used BL schemes (i.e. the Yonsei University (YSU) [Hong et al., 2006; Hu et al., 2013], Mellor–Yamada–Janjic (MYJ) [Janjić, 1994], Bougeault – Lacarrere (Boulac) [Bougeault and Lacarrére, 1989] and Asymmetric Convective Model, version 2 (ACM2) [Pleim, 2007] schemes) were tested. It was found that the selection of the BL scheme does not affect the simulation of local atmospheric circulations. The simulation results with the YSU scheme will be presented in this manuscript.

The other physics parameterization schemes employed in this study include the updated rapid radiative radiation scheme [Iacono et al., 2008], and the Noah land surface scheme [Chen and Dudhia, 2001] with a single-layer urban canopy model [Kusaka et al., 2001; Kusaka and Kimura, 2004]. The parameters in the urban canopy model are set following the configurations used in previous urban studies for the BTH region [Wang et al., 2012; 2013].

Considering that the real situation of atmospheric pollution is complicated, which is modulated by the cloud processes, BL processes, and transient processes (i.e. fronts, troughs). To understand the complex contributions of these various processes, it is necessary to develop first a complete understanding of effects the BL processes in a clear condition. Thus, the microphysics and cumulus schemes are thus turned off in the idealized simulations. Similar approaches to isolate the BL process from moist process have been used by De Wekker [2008] to investigate the suppression of BLH near a mountain, and by Pu and Dickinson [2014] to investigate the dynamics of Low-Level Jet over the Great Plains, and by Braun et al. [1999] to investigate barrier jet formation on the western side of a plateau. Besides, the BTH region locates in the semi-arid area of northern China where the annual precipitation is merely 570 mm [Gong et al., 2004], and most pollution episodes occur on days without precipitation. Thus study of BL processes in a dry condition is most relevant in this region for air pollution purpose.

The overarching goal of the current study is to examine the seasonal mean diurnal cycle of BL processes/structure. To this end, the four idealized simulations are initialized with seasonal mean meteorological conditions at 0000 UTC, and forced by seasonal mean (but with diurnal variations) lateral boundary conditions and solar radiation in 2010. The year 2010 is chosen because the seasonal synoptic forcing in this year is quite similar to the mean seasonal synoptic forcing during the past three decades. To represent the seasonal mean solar radiation forcing, the four simulations are initialized at 0800 LT (0000 UTC) on a day in the middle of each season, i.e., 14 January, 14 April, 14 July, and 14 October, respectively. The seasonal mean boundary and initial conditions for the atmosphere, ocean, and soil are derived from the National Center for Environmental Prediction (NCEP) global Final (FNL) analysis from December 2009 to November 2010. The lateral boundary conditions are derived from average FNL analyses at 0000, 0600, 1200, and 1800 UTC for each season. These seasonal mean boundary conditions are cycled periodically in time (i.e., from 0000 to 0600 to 1200 to 1800 UTC and then back to 0000 UTC), allowing diurnal variation (but not other transient atmospheric processes such as fronts, troughs and potential vorticity anomalies) to influence the simulation domain [Trier et al., 2010; Sun and Zhang, 2012]. A similar approach to set up the initial and boundary conditions has been used in previous studies to investigate diurnal variations of precipitation in China [Sun and Zhang, 2012] and United States [Trier et al., 2010]. The simulations are run for 40 hours, and the sea surface temperature is updated every 6 hours. The first 16 hours of each simulation are considered as a spin-up period, and the remaining 24 hours (from 0000 LT to 2400 LT) are used to investigate the seasonal mean diurnal variation of BL processes/structure. The effect of different spin-up times (16 hours and 28 hours) was tested, it was found that the selection of spin-up time does not affect the simulations of local atmospheric circulations.

Our approach differs from that of Lu et al. [2010] and Wu et al. [2011] in terms of the configuration of lateral boundary conditions. Lu et al. [2010] and Wu et al. [2011] used time-independent seasonal mean lateral boundary conditions (i.e., without diurnal variation) in their model simulations to investigate the diurnal cycle of sea-breeze and urban heat island effects in the Pearl River Delta region of China. Such boundary conditions removed the diurnal cycle of atmospheric properties at the model boundaries, possibly suppressing the diurnal cycle of BL processes/structures in the domain in Lu et al. [2010] and Wu et al. [2011]. This negative effect is avoided in our simulations by using seasonal mean boundary conditions with diurnal variations.

2.2 Data for model evaluation and analysis of BL processes

Observations of 2-m temperature and relative humidity (RH) archived in the National Climatic Data Center (NCDC) data are extracted to evaluate the performance of the model in this study. See the location of NCDC stations in Figure 1a.

Since 2004, a dense network of automatic weather stations (AWS) has been deployed in Beijing area by the Beijing Meteorological Bureau, which provides hourly observations of air temperature, relative humidity, wind speed, and wind direction [Yang et al., 2013; Dou et al., 2015]. In this study, the observations of the AWS network from 2010 to 2011 are used to investigate the seasonal variation of BL processes in Beijing.

Fine-resolution radiosonde profiles at the Nanjiao site (39.8 ^{o}N, 116.467 ^{o}E) in Beijing are also used to demonstrate the impact of MPC on BL structure on 12 September, 2010. Such a case study is presented in the supplementary file.

3. Results

3.1 Large scale forcing and thermal conditions

Comparison of the seasonal mean 850-hPa geopotential height fields (Figure 2) illustrates a distinctively different synoptic pattern in summer, with a high pressure synoptic system (the subtropical anticyclone) located to the southeast of the BTH region and a low pressure system to the northwest (Figure 2b). Such a synoptic pattern supports a southerly synoptic wind and southeasterly BL prevailing wind in the BTH region. In other three seasons, a northeast-to-southwest pressure gradient persists in the BTH region (Figures 2a, 2c and 2d), supporting a northwesterly synoptic wind in BTH. Impact of the different seasonal synoptic forcing on BL processes/structure in BTH will be examined using the four idealized simulations.

Simulated seasonal mean 2-m temperature and RH fields at 1400 LT are compared with the observation archived by NCDC (Figures 3, 4). Even though cloud processes are excluded, the idealized simulations successfully reproduce the general surface temperature and RH distribution of each season. The correlation between the observed and simulated 2-m temperature is significant, with a correlation coefficient of 0.96 ($p < 0.01$). The simulated 2-m RH also agrees well with the observation (Figure 4), with a correlation coefficient of 0.73 ($p < 0.01$). The good model performance in terms of spatial distribution of temperature and RH provides a basis for the model to capture seasonal variation of thermally-induced BL processes. The daily maximum 2-m temperature in BTH is ~296 K (spring), 310 K (summer), 295 K (fall), 274 K (winter), respectively. The combination of high temperature and strong solar radiation during the summer provides favorable conditions for ozone formation in the BL, which resulted in frequent severe ozone pollution events in summer in BTH [Zhang et al., 2015b; Wang et al., 2011; Xu et al., 2011; Xu et al., 2008].

Unlike ozone, which is significantly correlated with temperature and solar radiation, ambient $PM_{2.5}$ concentrations in BTH appear to be dictated by more complex factors [Zhang et al., 2015b; Wang et al., 2011; Xu et al., 2011; Xu et al., 2008]. Recent studies [Quan et al., 2013; Sun et al., 2013; Tie et al., 2014] have suggested that BL processes/structure may play an important role in modulating the $PM_{2.5}$ concentrations in this region. Since $PM_{2.5}$-dominated haze pollution episodes in the BTH region occur mostly during the fall and winter [Fu et al., 2014], the local atmospheric circulations and BL structure in these two seasons are presented first, followed by spring and summer.

3.2 Local atmospheric circulations and BL structure during fall

In fall, a momentum front develops around 1000 LT along the coast of the Bohai Sea and begins to move inland (Figures 5a-d). Behind the momentum front, the air is moister (Figures 5i-l) and cooler (Figures 5m-p) than in the continental air mass ahead of the front. These sharp changes across the front suggest a typical marine air mass behind the front. The inland penetration of cool, moist marine air in the form of a front indicates the development of a sea-breeze circulation along the Bohai Bay. At the leading edge of the sea-breeze front (SBF), due to the sharp change of wind speed, a convergence belt with strong upward motion (Figures 5e-h) is present, indicating the sea-breeze head [Miller, et al., 2003].

During the rest of the day, as the thermal difference between the land and sea persists (Figure S2) and strengthens, the SBF advances further inland as the sea-breeze circulation intensifies (Figure 5). The development and inland penetration of the sea-breeze are further illustrated in the vertical cross-section of wind across the sea-breeze front (Figure 6). The onshore flow, upward motion at the SBF, and a return offshore flow above 300 m are prominent at 1200 LT, indicating a complete sea-breeze circulation cell. The upward motion induced by the convergence at the SBF lifts the BL top during the daytime. At 1500 LT, the sea-breeze head lifts the

BL at Tianjin as high as ~2 km (Figure 6b). The vertical motion in the coastal area peaks around 1500 LT when the thermal contrast between land (warm) and sea (cool) is the strongest, and the vertical motion weakens gradually afterward (Figure S5).

After sunset, the land-sea thermal contrast is reduced, but due to the inertia effect, the SBF continues to move inland until 2200 LT, reaching as far as ~100 km from the coast (Figures 5d, 5h, 5l, 5p and 5d). Afterward, as radiation cooling persists, the thermal contrast between the land and the sea reverses (i.e., the air temperature over the land is lower than air temperature over the sea), causing the sea-breeze to gradually weaken, and ultimately transition to an offshore land-breeze by around 0200 LT in the coastal area. The nighttime and early morning offshore land-breeze may bring the BTH pollutants over the sea and the afternoon onshore sea-breeze may bring those pollutants back to the coastal area. The land- and sea-breeze diurnal reversal provides a mechanism for the pollutants emitted in the coastal cities to be recycled and accumulated (see the transport of pollutants by land/sea breeze in Figures S6c-d), as reported in previous studies [Simpson, 1994; Grossi et al., 2000; Baumgardner et al., 2006; Levy et al., 2009]. Such a mechanism has been illustrated to exacerbate air pollution during a $PM_{2.5}$ dominated haze episode in the BTH region [Sun et al. 2013].

In addition to the sea-breeze circulation, another local atmospheric circulation develops over Beijing and the adjacent mountains (Figure 6) in fall. During the daytime in warm seasons, mountains act as elevated heat sources [Banta and Cotton, 1981]. The near-surface air over the mountains is heated by the strong sensible heat flux (Figure S3), resulting in a higher air temperature than that at the same height over the adjacent plains (Figures S4, 7a). Such a thermal contrast causes thermally-induced upslope winds to develop along the sloping terrain. A return flow simultaneously develops above the BL (Figure 6a). Such a closed circulation cell indicates the MPC. The MPC cell develops in the morning with a horizontal scale of ~50 km at 1200 LT and grows with a horizontal scale of ~80 km at 1500 LT (Figure 6b).

In the afternoon, the return flow of the MPC, superimposed on the prevailing northwesterly wind, brings warmer air from the mountains to the adjacent plains (Figure 7), forming an inversion layer above the BL (Figure 8c) and suppressing the vertical growth of the BL. In addition, the downward motion of the return flow also suppresses the development of BL over the adjacent plain. As a result, the BLH in Beijing is merely ~0.9 km at 1500 LT (Figure 8c), which is significantly lower than the BLH further from the mountains at Langfang (~1.3 km) or Tianjin (~1.8 km). The spatial distribution of simulated BLH (Figure 9c) indicates that suppression of the BL occurs not only in Beijing, but throughout the western and northern part of the BTH region near the Taihang and Yan mountains. The BLH in this part of the region is limited to ~1 km during the afternoon (Figure 9c). Such a scenario (i.e., suppression of BL development by the MPC) is nicely observed using fine-resolution radiosonde data on 12 September 2010 (see Figure S7 and relevant discussion in the supplementary file). The shallow BL suppressed by MPC limits the total air volume available for dispersion of atmospheric pollutants, leading to accumulation of pollutants in the western plains of the BTH region (Figures 10c, 11c). Suppression of the convective BL near mountains and plateaus has been previously reported in limited short-term case studies [Hu et al., 2014; De Wekker, 2008], but its implications for seasonal variation of pollution in a region have not been explicitly investigated. To our knowledge, this study for the first time indicates that such processes may have be partially responsible for the high frequency of $PM_{2.5}$ dominated haze pollution events during the fall in the BTH region.

After sunset, the differential heating between the mountains and plains reverses: the near-surface air temperature over the mountains becomes lower than the air temperature at the same height over the adjacent plains (Figure 7d). As a result, a downslope mountain-breeze develops (Figures 6d). Such a diurnal variation of MPC in fall manifests itself in the diurnal reversal of surface wind direction over Beijing, i.e., with the southerly wind dominating in the afternoon (Figures S8g, S9) and the reversed northwesterly wind during nighttime (Figures S8c, S9). As the cold mountain air flows down the slope and accumulates in the adjacent plains during the night and early the next morning, a pool of cool air forms over the western plains of the BTH region (Figure 12). This pool of cool air is characterized by very stable stratification and weak turbulent mixing, favoring the accumulation of air pollutants. Similar cool air pools have been reported to form frequently near other mountains and plateaus due to similar mechanisms [e.g., Mahrt et al., 2010]. The cool air pool persists until the early morning (Figure 12d), and slows the growth of convective BL (Figure 7a) in the western plains of the BTH region. Therefore, the presence of the nighttime cool air pool also plays a role in limiting the convective BL development in this region as shown in Figure 9c.

3.3 Local atmospheric circulations and BL structure during winter

In winter, thermally-induced local atmospheric circulations are suppressed in the presence of weak surface sensible heat flux (Figures S1d, S3d) and strong northwesterly synoptic winds. The sea-breeze develops by around 1500 LT (Figures 13b, 13f), but barely advances inland during the afternoon (Figures 13c, 13g). After sunset, the sea-breeze subsides by around 2000 LT (Figures 13d, 13h). The maximum inland penetration distance of the sea-breeze in winter is only ~20 km (Figures 13c, 13g). On the western side of the BTH region, without sufficient heating from the solar radiation (Figures S3, S4), the wintertime MPC is sufficiently weak in the afternoon that it is almost swept out by the strong northwesterly prevailing wind (Figures 13, 14). As a result, northwesterly winds dominate near the surface in Beijing area throughout the day (Figures S8d, S8h, and S9).

Due to the weak surface sensible heat flux (Figure S1d), the development of daytime convective BL in winter is considerably limited (Figures 8d, 14) in the presence of a strong inversion layer capping the BL (Figures 8d, 14). As a result, the BLH over the whole BTH region reaches only ~1 km in the afternoon (Figures 8d, 9d). Such a low BLH over the whole BTH region limits the vertical dispersion of pollutants (Figures 10d, 11d) and is partially responsible for the frequent occurrence of severe regional air pollution events during the winter in this region [Wang et al., 2014a and 2014b]. Such a connection has also been suggested in a previous study [Schleicher et al. 2015], which ascribed the winter peak of daytime atmospheric mercury in Beijing to the seasonal low mixing layer height during the winter, in addition to seasonal sources of mercury.

3.4 Local atmospheric circulations and BL structure during summer

Unlike during the winter, intense solar radiation and long days during the summer favors the development of local atmospheric circulations. The sea-breeze develops in the early morning (around 0800 LT) and persists until midnight (Figure 15). By 2000 LT, the SBF propagates inland up to ~150 km from the coast and reaches the base of the mountains to the west of Beijing (Figures 15d, 15h and 16d). Such deep inland sea-breeze penetration is not only driven by the local thermal contrast between the land and the sea, but is also facilitated by the southeasterly prevailing wind in the BL (Figure 2b), which is oriented along the same axis as the sea-breeze. A case of sea-breeze development and inland penetration on July 20 2010 is analyzed using surface AWS observations in the supplementary materials (Figures S10, S11). The extent of inland penetration of sea-breeze during summertime is consistent with previous studies e.g., Liu et al. [2009] and Zhang et al. [2013].

In addition to the prominent sea-breeze, the MPC is also well established in the summer in the western BTH region (Figure 16). The upslope breeze appears by around 0800 LT and develops into a closed circulation by around noon (Figure 16a). Much like in the fall, the downward branch of the MPC suppresses vertical growth of the BL over the adjacent plains in the late morning (Figure 16a). However, unlike the fall case, the horizontal scale of the closed MPC circulation is limited to ~30 km in the afternoon due to perturbation by vigorous turbulent eddies over the mountains and plains (Figures 16b-c).

With the strong turbulent eddies (Figures 16b-c), the BL grows up to ~2 km over the plains in the afternoon in summer in most areas of the BTH region (Figures 8b, 9b and 16), except for the narrow coastal area (e.g., Tianjin) affected by the sea-breeze. The near-surface air temperature along the eastern coast of the BTH region is reduced to some extent by cool-air advection associated with the sea-breeze. As a result, the thermal turbulent motions are weakened and BLH is relatively low in coastal areas (Figure 9b). The relatively high daytime BLH over much of the BTH in summer (Figure 9b) favors the dispersion of pollutants in this region during the day (Figures 10b, 11b).

3.5 Local atmospheric circulations and BL structure during spring

In spring, the prevailing synoptic winds over the BTH region are northwesterly, much like in the fall and winter (Figures 2a, 2c, and 2d). BL processes and structure during spring, however, are different from those during fall and winter (Figures 17, 18, 19). Compared to other seasons, the synoptic forcing indicated by the wind at ~3 km AGL during the spring (Figures 17a, 17e) is stronger than that of summer and fall (Figures 17b, 17c, 17f and 17g), but weaker than that of winter (Figures 17d, 17h). It is interesting that even though the synoptic wind in spring is weaker than that of winter, the BL wind in spring is stronger than that of winter (Figures 17e, 17h). Such wind speed differences between spring and winter are consistent with the seasonal mean wind difference derived from the ERA-interim data during the past three decades (not shown). The strong BL wind in spring seen in this study is consistent with previous studies [e.g., Liu et al., 2009a; Zhang, 2015a; Zhao et al., 2009; and Guo et al., 2011], which report that the strongest surface winds in the BTH region occur during the spring.

The distinct differences in vertical distribution of wind speeds between spring and winter can be explained by the impacts of different atmospheric stability on downward transport of free tropospheric momentum. In winter, as discussed earlier, a strong inversion layer forms over the BL in the presence of weak solar radiation (Figure 14), inhibiting the downward transport of free tropospheric momentum. As a result, the wintertime BL is effectively decoupled from the free troposphere (Figure 17h). Due to a similar mechanism, wintertime BL/free troposphere decoupling has been reported to occur in many places, including the Colorado Plateau [Bana and Cotton, 1981; Whiteman et al., 1999], the Cascade Mountains of Oregon [Daly et al., 2010] in United States, and Scott Base in Antarctica [Sinclair, 1988]. During spring, in the presence of relatively stronger solar radiation and surface sensible heat flux (Figure S1), the stability above the BL is substantially reduced (Figures 14, 19). As a result, free tropospheric momentum is actively transported downward into the BL (Figure 17), leading to an annual maximum in surface wind speed, as reported in previous studies [e.g., Liu et al., 2009a; Zhang, 2015a; Zhao et al., 2009; and Guo et al., 2011]. In the presence of strong mechanical forcing in the BL, the sea-breeze circulation is confined to the eastern coastal area (Figure 18), while the MPC does not develop on the western side of the BTH region (Figures 17e, 19).

Due to the strong wind shear associated with the strong mechanical forcing above the surface, the BLH over the whole BTH region increases to as much as ~2.5 km during the daytime in spring (Figures 8a, 9a). The high BLH and strong BL wind over the BTH region in spring favor the dispersion of locally emitted pollutants (Figures 10a, 11a). Pollutants emitted in the BTH may be advected over the Bohai Sea by the northwesterly synoptic wind in the evening and morning, but they may be recycled and accumulated in the narrow coastal region in the afternoon in the presence of confined sea-breeze circulation (Figures S6a-b). On the other hand, the strong northwesterly wind may promote lofting of dust from the Gobi Desert (Figure 1a) when the seasonal soil moisture is low in spring, and subsequent transport of the lofted dust into the BTH region [Zhao et al., 2007; Sun et al., 2000; Xie et al., 2005].

4. Conclusions and discussion

In this study, the seasonal variation of local atmospheric circulations and BL structures and its impacts on air quality in the BTH region are examined using four idealized WRF-Chem tracer simulations with meteorological conditions initialized using seasonally-averaged analyses and laterally forced by seasonally averaged analyses every 6 h (thus including diurnal variations). This configuration mitigates the effects of transient synoptic forcing originating upstream of the model domain, allowing the simulations to capture the diurnal cycle of seasonal mean BL processes and structures in the absence of transient synoptic disturbances. The simulation results illustrate how seasonal variations of thermal conditions and synoptic patterns significantly modulate BL processes/structure, and air quality subsequently.

In fall, during the afternoon, differential heating between the mountains (warmer) and plains (relatively cooler) in the presence of relatively weak northwesterly synoptic forcing leads to a prominent mountain-plain breeze circulation (MPC). The downward motion associated with the MPC, together with the warm advection from the mountains, suppresses BL development over the western plains of the BTH region. On the eastern side of the BTH region, due the thermal contrast between the land (warm) and sea (cool), a sea-breeze circulation develops late in the morning and grows in the afternoon. The sea-breeze front lift the BL top as high as ~2 km over Tianjin during the afternoon. At night during the fall, a cool air pool forms in the western plains of the BTH region in the presence of a downslope mountain breeze. This cool air pool persists until the next morning and slows the development of the daytime convective BL. These typical BL processes in fall exacerbate local air pollution in the western part of the BTH region (e.g., Beijing), and must be partially responsible for the frequent occurrence of air pollution events in fall in this region.

In summer, in the presence of southeasterly BL prevailing wind, intense solar radiation, the sea-breeze front penetrates inland as far as ~150 km, while the horizontal scale of MPC cell is reduced comparing to fall due to the perturbation by vigorous turbulent eddies over the mountains and plains.

In spring and winter the region experiences strong northwesterly synoptic winds; during these seasons, the sea-breeze circulation is confined in the coastal area and the MPC is suppressed. The BLH is low in winter due to strong near-surface stability; in spring the BL grows quite high due to strong mechanical forcing. In winter, low BLH throughout the day favors the occurrence of heavy regional haze pollution.

As a result of the seasonal variation of the BL processes and structures mentioned above, the daytime BLH over most of the BTH region follows a downward trend from spring to winter, i.e., spring > summer > fall > winter, leading to the best dispersion condition in spring and worse dispersion condition in fall and winter.

The new knowledge of seasonal variations of BL processes/structures and dispersion conditions obtained during this study has important implications for better identifying the essential meteorological factors for pollution episodes, and for forecasting air pollution in the BTH region. This study suggests that, when investigating air pollution in this region, local atmospheric circulations and their impacts on BL structure should be carefully considered alongside other meteorological and chemical factors.

Although the important implications of BL processes and structures on seasonal variation of pollution levels in the BTH region have been emphasized in this study, the important role of seasonal variations in emissions on modulation of the seasonal air quality in this region [He et al., 2006; Zhang et al., 2013; Schleicher et al., 2015; Zhao et al., 2009] cannot be deemphasized.

Acknowledgements

We thank the Beijing Meteorological Bureau for providing the auto weather station (AWS) data. This work was supported by the National Natural Science Foundation of China (Grant No. 41175004, 41465001, 41375109), the China Meteorological Administration Special Public Welfare Research Fund (GYHY201106033), the China Scholarship Council, Key Laboratory of Meteorological Disaster of Ministry of Education，Nanjing University of Information Science and Technology (KLME1412), and National 973 Fundamental Research Program of China (Grant No. 2013CB430103). Proofreading by Nate Snook is greatly appreciated. Model data presented in this study have been archived at Center for Analysis and Prediction of Storms, University of Oklahoma, and are available from the authors upon request. The AWS data are archived by the Beijing Meteorological Bureau, and the radiosonde data are archived by the China Metrological Administration (CMA), which are available upon request with the permission from those agencies. The NCDC data used for model evaluation are downloaded from http://www7.ncdc.noaa.gov/CDO/cdo

References

An, X., T. Zhu, Z. Wang, and Y. Wang (2007), A modeling analysis of a heavy air pollution episode occurred in Beijing, *Atmos. Chem. Phys.*, 7, 3103–3114, doi:10.5194/acp-7-3103-2007.

Banta, R, and W. R. Cotton (1981), An Analysis of the Structure of Local Wind Systems in a Broad Mountain Basin. *J. Appl. Meteor.*, 20, 1255–1266, doi: http://dx.doi.org/10.1175/1520-0450(1981)020<1255:AAOTSO>2.0.CO;2

Baumbach, G., and U. Vogt (1999), Experimental determination of the effect of mountain-valley breeze circulation on air pollution in the vicinity of Freiburg, *Atmos. Environ.*, 33(24-25), 4019-4027, doi:10.1016/S1352-2310(99)00143-0.

Baumgardner, D., G. B. Raga, M. Grutter, and G. Lammel (2006), Evolution of anthropogenic aerosols in the coastal town of Salina Cruz, Mexico: Part I particle dynamics and land–sea interactions, *Sci. Total Environ.*, 367(1), 288-301, doi:10.1016/j.scitotenv.2005.11.013.

Bougeault, P., and P. Lacarrére (1989), Parameterization of orography- induced turbulence in a mesobeta-scale model, *Mon. Weather Rev.*, 117, 1872–1890, doi:10.1175/1520-0493(1989)117<1872:POOITI>2.0. CO;2

Braun, S. A., R. Rotunno, and J. B. Klemp (1999), Effects of Coastal Orography on Landfalling Cold Fronts. Part I: Dry, Inviscid Dynamics, *J. Atmos. Sci.*, 56(4), 517–533, doi:10.1175/1520-0469(1999)056<0517:EOCOOL>2.0.CO;2.

Buckley, R. L., and R. J. Kurzeja (1997), An Observational and Numerical Study of the Nocturnal Sea Breeze. Part I: Structure and Circulation. *J. Appl. Meteor.*, 36, 1577–1598, doi: http://dx.doi.org/10.1175/1520-0450(1997)036<1577:AOANSO>2.0.CO;2.

Chan, C. K., and X. H. Yao (2008), Air pollution in mega cities in China, *Atmos. Environ.*, 42, 1-42, doi:10.1016/j.atmosenv.2007.09.003.

Chen, F., and J. Dudhia (2001), Coupling an advanced land-surface/ hydrology model with the Penn State/ NCAR MM5 modeling system. Part I: Model description and implementation, *Mon. Wea. Rev.*, 129(4), 569-585, doi: http://dx.doi.org/10.1175/1520-0493(2001)129<0569:CAALSH>2.0.CO;2.

Chen, P. F., J. N. Quan, Q. Zhang, X. X. Tie, Y. Gao, and X. Li (2013), Measurements of vertical and horizontal distributions of ozone over Beijing from 2007 to 2010, *Atmos. Environ.*, 74, 37–44, doi:10.1016/j.atmosenv.2013.03.026.

Chen, Y., C. S. Zhao, Q. Zhang, Z. Z. Zhao, M. Y. Huang, and X. C. Ma (2009), Aircraft study of mountain chimney effect of Beijing, China, *J. Geophys. Res. Atmos.*, 114(D8), doi: 10.1029/2008JD010610.

Daly, C., D. R. Conklin, and M. H. Unsworth (2010), Local atmospheric decoupling in complex topography alters climate change impacts, *Int. J. Climatol.*, 30, 1857–1864, doi: 10.1002/joc.2007.

De Wekker, S. F. J. (2008), Observational and numerical evidence of depressed convective boundary layer height near a mountain base, *J. Appl. Meteor. Climatol.*, 47, 1017–1026, doi: http://dx.doi.org/10.1175/2007JAMC1651.1.

Dou, J., Y. Wang, R. Bornstein, and S. Miao (2015), Observed Spatial Characteristics of Beijing Urban Climate Impacts on Summer Thunderstorms, *J. Appl. Meteorol.*

Climatol., *54*(1), 94–105, doi:10.1175/JAMC-D-13-0355.1

Eisinger, M., and J. P. Burrows (1998), Tropospheric sulfur dioxide observed by the ERS-2 GOME instrument, Geophys Res Lett, 25(22), 4177-4180, Doi 10.1029/1998gl900128.

Fiedler, V., R. Nau, S. Ludmann, F. Arnold, H. Schlager, and A. Stohl (2009), East Asian SO2 pollution plume over Europe - Part 1: Airborne trace gas measurements and source identification by particle dispersion model simulations, Atmos Chem Phys, 9(14), 4717-4728.

Fu, G. Q., W. Y. Xu, R. E. Yang, J. B. Li, and C. S. Zhao (2014), The distribution and trends of fog and haze in the North China Plain over the past 30 years, *Atmos. Chem. Phys.*, 14, 11949-11958, doi: 10.5194/acp-14-11949-2014.

Gao, J., H. Tian, K. Cheng, L. Lu, M. Zheng, S. Wang, J. Hao, K. Wang, S. Hua, C. Zhu, and Y. Wang (2015), The variation of chemical characteristics of PM2.5 and PM10 and formation causes during two haze pollution events in urban Beijing, China, *Atmos. Envrion.*, doi: 10.1016/j.atmosenv.2015.02.022.

Gohm, A., F. Harnisch, J. Vergeiner, F. Obleitner, R. Schnitzhofer, A. Hansel, A. Fix, B. Neininger, S. Emeis, and K. Schäfer (2009), Air Pollution Transport in an Alpine Valley: Results From Airborne and Ground-Based Observations, *Bound-Layer Meteorol.*, 131(3), 441-463, doi: 10.1007/s10546-009-9371-9.

Gong, D.-Y., P.-J. Shi, and J.-A. Wang (2004), Daily precipitation changes in the semi-arid region over northern China, *J. Arid Environ.*, 59(4), 771–784, doi:10.1016/j.jaridenv.2004.02.006.

Grell, G. A., S. E. Peckham, R. Schmitz, S. A. McKeen, G. Frost, W. C. Skamarock, and B. Eder (2005), Fully coupled "online" chemistry within the WRF model, *Atmos. Environ.*, 39(37), 6957–6975, doi:10.1016/j.atmosenv.2005.04.027.

Grossi, P., P. Thunis, A. Martilli, and A. Clappier (2000) Effect of Sea Breeze on Air Pollution in the Greater Athens Area. Part II: Analysis of Different Emission Scenarios. *J. Appl. Meteor.*, 39, 563–575, doi: http://dx.doi.org/10.1175/1520-0450(2000)039<0563:EOSBOA>2.0.CO;2

Guo, H., M. Xu, and Q. Hu (2011), Changes in near-surface wind speed in China: 1969–2005, *Int. J. Climatol.*, 31, 349–358, doi: 10.1002/joc.2091.

He, K. B., F. M. Yang, Y. L. Ma, Q. Zhang, X. H. Yao, C. K. Chan, S. Cadle, T. Chan, and P. Mulawa (2001), The characteristics of PM2.5 in Beijing, China, *Atmos. Environ.*, 35, 4959-4970, doi:10.1016/S1352-2310(01)00301-6.

He, L. Y., M. Hu, X. F. Huang, Y. H. Zhang, and X. Y. Tang (2006), Seasonal pollution characteristics of organic compounds in atmospheric fine particles in Beijing, *Sci. Total Environ.*, 359, 167-176, doi:10.1016/j.scitotenv.2005.05.044.

Hong, S. Y., Y. Noh, and J. Dudhia (2006), A new vertical diffusion package with an explicit treatment of entrainment processes, *Mon. Wea. Rev.*, 134, 2318-2341, doi: http://dx.doi.org/10.1175/MWR3199.1.

Hu, X. M., Z. Q. Ma, W. L. Lin, H. L. Zhang, J. L. Hu, Y. Wang , X. B. Xu, J. D. Fuentes, and M. Xue (2014), Impact of the Loess Plateau on the atmospheric boundary layer structure and air quality in the North China Plain: A case study, *Sci. Total Environ.*, 499, 228-237, doi:10.1016/j.scitotenv.2014.08.053.

Hu, X. M., P. M. Klein, and M. Xue (2013), Evaluation of the updated YSU planetary boundary layer scheme within WRF for wind resource and air quality assessments, *J. Geophys. Res. Atmos.*, 118(10), 490-505, doi: 10.1002/jgrd.50823.

Hu, X. M., J. W. Nielsen-Gammon, and F. Zhang (2010), Evaluation of three planetary boundary layer schemes in the WRF model, *J. Appl. Meteorol. Climatol.*, 49(9), 1831–1844, doi:10.1175/2010JAMC2432.1.

Huang, R. J., Y. Zhang, C. Bozzetti, K. F. Ho, J. J. Cao, Y. Han, K. R. Daellenbach, J. G. Slowik, S. M. Platt, F. Canonaco, P. Zotter, R. Wolf, S. M. Pieber, E. A. Bruns, M. Crippa, G. Ciarelli, A. Piazzalunga, M. Schwikowski, G. Abbaszade, J. Schnelle-Kreis, R. Zimmermann, Z. An, S. Szidat, U. Baltensperger, I. El Haddad and A. S. H. Prévôt (2014), High secondary aerosol contribution to particulate pollution during haze events in China, *Nature*, 514, 218-222, doi:10.1038/nature13774.

Iacono, M. J., J. S. Delamere, E. J. Mlawer, M. W. Shephard, S. A. Clough, and W. D. Collins (2008), Radiative forcing by long‐lived greenhouse gases: Calculations with the AER radiative transfer models, *J. Geophys. Res. Atmos.*, 113 (D13), doi:10.1029/2008JD00994.

Janjić, Z. I. (1994), The step-mountain Eta coordinate model: Further development of the convection, viscous sublayer and turbulent closure schemes, *Mon. Weather Rev.*, 122, 927–945, doi:10.1175/1520-0493 (1994)122<0927:TSMECM>2.0.CO;2..

Ji, D., L. Li, Y. Wang, J. Zhang, M. Cheng, Y. Sun, Z. Liu, L. Wang, G. Tang, B. Hu, N. Chao, T. Wen, and H. Miao (2014), The heaviest particulate air-pollution episodes occurred in northern China in January, 2013: Insights gained from observation, *Atmos. Environ.,* 92, 546-556, doi:10.1016/j.atmosenv.2014.04.048.

Kurosaki, Y., and M. Mikami (2003), Recent frequent dust events and their relation to surface wind in East Asia, *Geophys. Res. Lett.*, 30 (14), 1736, doi:10.1029/2003GL017261.

Kusaka, H., and F. Kimura (2004), Coupling a single-layer urban canopy model with a simple atmospheric model: Impact on urban heat island simulation for an idealized case, *J. Meteor. Soc. Japan*, 82, 67-80, doi: http://dx.doi.org/10.2151/jmsj.82.67.

Kusaka, H., H. Kondo, Y. Kikegawa, and H. Kimura (2001), A simple single-layer urban canopy model for atmospheric models: Comparison with multi-layer and slab models, *Bound-Layer Meteorol.*, 101, 329-358, doi:10.1023/A:1019207923078.

Liu, H. P., and J. C. L. Chan (2002), Boundary layer dynamics associated with a severe air-pollution episode in Hong Kong, *Atmos. Environ.*, 36, 2013-2025, doi:10.1016/S1352-2310(02)00138-3.

Liu, S., J. Qiu, and X. Mo (2009a), Wind Velocity Variation from 1951 to 2006 in the North China Plain, *Resources Science (in Chinese)*, 31(9), 1486-1492, doi:10.3321/j.issn:1007-7588.2009.09.005.

Liu, S. H., Z. X. Liu, J. Li, Y. C. Wang, Y. J. Ma, L. Sheng, H. P. Liu, F. M. Liang, G. J. Xin, and J. H. Wang (2009b), Numerical simulation for the coupling effect of local atmospheric circulations over the area of Beijing, Tianjin and Hebei provinces. *Sci. China Ser. D*, 52(3), 382-392, doi: 10.1007/s11430-009-0030-2.

Liu, X. G., J. Li, Y. Qu, T. Han, L. Hou, J. Gu, C. Chen, Y. Yang, X. Liu, T. Yang, Y. Zhang, H. Tian, and M. Hu (2013), Formation and evolution mechanism of regional haze, a case study in megacity Beijing, China, *Atmos. Chem. Phys*., 13(9), 4501-4514, doi:10.5194/acp-13-4501-2013.

Levy, I., Y. Mahrer, and U. Dayan (2009), Coastal and synoptic recirculation affecting air pollutants dispersion: a numerical study. *Atmos. Environ.*, 43(12), 1991-1999, doi:10.1016/j.atmosenv.2009.01.017.

Lo, J. C. F., A. K. H., J. C. H. Fung, and F. Chen (2006), Investigation of enhanced cross-city transport and trapping of air quality by coastal and urban land-sea breeze circulations, *J. Geophys. Res. Atmos.*, 111(D14), doi: 10.1029/2005JD006837.

Lu, R., and R. P. Turco (1994), Air pollutant transport in a coastal environment. Part I: Two-deimensional simulations of sea-breeze and mountain effects, *J. Atmos. Sci*., 51(15), 2285-2308, doi:http://dx.doi.org/10.1175/1520-0469(1994)051<2285:APTIAC>2.0.CO;2.

Lu, X., K. C. Chow, T. Yao, A. K. H. Lau, and J. C. H. Fung (2010), Effects of urbanization on the land sea breeze circulation over the Pearl River Delat region in winter, *Int. J. Climatol.*, 30, 1089-104, doi:10.1002/joc.1947.

Mahrt, L., S. Richardson, N. Seaman, and D. Stauffer (2010), Non-stationary drainage flows and motions in the cold pool. *Tellus A*, 62(5), 698-705, doi:10.1111/j.1600-0870.2010.00473.x.

Miao, Y., S. Liu, Y. Zheng, S. Wang, and B. Chen (2015a), Numerical Study of the

Effects of Topography and Urbanization on the Local Atmospheric Circulations over the Beijing-Tianjin-Hebei, China, *Adv Meteorol*, *2015*, 16, doi:10.1155/2015/397070.

Miao, Y, S. Liu, Y. Zheng Y, S. Wang, B. Cheng, H. Zheng, and J. Zhao (2015b), Numerical study of the effects of local atmospheric circulations on a pollution event over Beijing-Tianjin-Hebei, China, *J. Environ. Sci*., doi: http://dx.doi.org/10.1016/j.jes.2014.08.025.

Miller, S. T. K., B. D. Keim, R. W. Talbot, and H. Mao (2003), Sea breeze: structure, Forecasting, and Impacts, *Rev. Geophys*., 41(3), doi:10.1029/2003RG000124

National Bureau of Statistics of China (NBSC) (1999-2011), China Statistics Yearbook. China Statistics Press, Beijing.

Pleim, J. E. (2007), A combined local and nonlocal closure model for the atmospheric boundary layer. Part I: Model description and testing, *J. Appl. Meteorol. Climatol.*, 46, 1383–1395, doi:10.1175/JAM2539.1.

Pu, B., and R. E. Dickinson (2014), Diurnal spatial variability of Great Plains summer precipitation related to the dynamics of the low-level jet, *J. Atmos. Sci.*, 71, 1807–1817, doi:10.1175/JAS-D-13-0243.1.

Puygrenier, V., F. Lohou, B. Campistron, F. Saïd, G. Pigeon, B. Bénech, and D. Serça, (2005), Investigation on the fine structure of sea-breeze during ESCOMPTE experiment, *Atmos. Res.*, 74(1-4), 329-353, doi:10.1016/j.atmosres.2004.06.011.

Qian, T. T., C. C. Epifanio, and F. Q. Zhang (2009), Linear Theory Calculations for the Sea Breeze in a Background Wind: The Equatorial Case, *J Atmos Sci*, *66*(6), 1749-1763, Doi 10.1175/2008jas2851.1.

Qu, W., J. Wang, X. Zhang, Z. Yang, and S. Gao (2015), Effect of cold wave on winter visibility over eastern China, *J. Geophys. Res.,* doi:10.1002/2014JD021958.

Quan, J., X. Tie, Q. Zhang, Q. Liu, X. Li, Y. Gao, and D. Zhao (2014), Characteristics of heavy aerosol pollution during the 2012-2013 winter in Beijing, China, *Atmos. Environ.*, 88, 83-89, doi:10.1016/j.atmosenv.2014.01.058.

Quan, J., Y. Gao, Q. Zhang, X. Tie, J. Cao, S. Han, J. Meng, P. Chen, and D. Zhao (2013), Evolution of planetary boundary layer under different weather conditions, and its impact on aerosol concentrations, *Particuology*, 11(1), 34-40, doi:10.1016/j.partic.2012.04.005.

Reible, D. D., J. E. Simpson, and P. F. Linden (1993), The sea breeze and gravity-current frontogenesis, *Q. J. Roy. Meteor. Soc.*, 119 (509), 1-16, doi:10.1002/qj.49711950902.

Reuten, C., D. G. Steyn, K. B. Strawbridge, and P. Bovis (2005), Observations of the relation between upslope flows and the convective boundary layer in steep terrain, *Bound-Layer Meteorol.*, 116(1), 37-61, doi:10.1007/s10546-004-7299-7.

San Martini, F. M., C. A. Hasenkopf, and D. C. Roberts (2015), Statistical analysis of PM2.5 observations from diplomatic facilities in China, *Atmos. Environ.*, 110, 174–185, doi:10.1016/j.atmosenv.2015.03.060.

Schleicher, N.J., J. Schäfer, G. Blanc, Y. Chen, F. Chai, K. Cen, and S. Norra (2015), Atmospheric particulate mercury in the megacity Beijing: Spatio-temporal variations and source apportionment, *Atmos. Environ.*, doi:10.1016/j.atmosenv.2015.03.018.

Shao, Y., and C. H., Dong (2006), A review on East Asian dust storm climate, modelling and monitoring, *Global Planet Change*, 52, 1–22, doi:10.1016/j.gloplacha.2006.02.011.

Simpson, J. E. (1994). Sea breeze and local winds. Cambridge University Press.

Sinclair, M. R. (1988), Local topographic influence on low-level wind at Scott Base, Antarctica, *New Zealand Journal of Geology and Geophysics*, 31(2), 237-245, doi: 10.1080/00288306.1988.10417772.

Sun, J. and F. Zhang (2012), Impacts of Mountain–Plains Solenoid on Diurnal Variations of Rainfalls along the Mei-Yu Front over the East China Plains, *Mon. Wea. Rev.*, 140, 379–397, doi: http://dx.doi.org/10.1175/MWR-D-11-00041.1

Sun, J., T. Liu, and Z. Lei (2000), Sources of heavy dust fall in Beijing, China on April 16, 1998. *Geophys. Res. Lett.*, 27(14), 2105-2108, doi: 10.1029/1999GL010814.

Sun, Y., S. Tao, G. Tang, and Y. Wang (2013), The vertical distribution of PM2.5 and boundary structure during summer haze in Beijing, *Atmos. Envrion.*, 74, 413-421, doi:10.1016/j.atmosenv.2013.03.011.

Sun, Y., G. Zhuang, A. Tang, Y. Wang, and Z. An (2006), Chemical Characteristics of PM2.5 and PM10 in Haze-Fog episodes in Beijing, Environ. Sci. Technol., 40, 3148-3155, doi: 10.1021/es051533g.

Tao, M., L. Chen, L. Su, and J. Tao (2012), Satellite observation of regional haze pollution over the North China Plain, *J. Geophys. Res. Atmos.*, 117(D12), doi:

10.1029/2012JD017915.

Tian, G., Z. Qiao, and X. Xu (2014), Characteristics of particulate matter (PM10) and its relationship with meteorological factors during 2001-2012 in Beijing, *Environ. Pollut.,* 192, 266-274, doi:10.1016/j.envpol.2014.04.036.

Tie, X., Q. Zhang, H. He, J. Cao, S. Han, Y. Gao, X. Li, and X. C. Jia (2014), A budget analysis of the formation of haze in Beijing, *Atmos. Environ.*, 100, 25-36, doi:10.1016/j.atmosenv.2014.10.038.

Tijm, A. B. C., A. A. M. Holtslag, and A. J. van Delden (1999), Observations and Modeling of the Sea Breeze with the Return Current. *Mon. Wea. Rev.*, 127, 625–640. doi: http://dx.doi.org/10.1175/1520-0493(1999)127<0625:OAMOTS>2.0.CO;2.

Trier, S. B., C. A. Davis, and D. A. Ahijevych (2010), Environmental Controls on the Simulated Diurnal Cycle of Warm-Season Precipitation in the Continental United States. *J. Atmos. Sci.*, 67, 1066–1090. doi: http://dx.doi.org/10.1175/2009JAS3247.1

van Donkelaar, A., R. V. Martin, M. Brauer, R. Kahn, R. Levy, C. Verduzco, and P. J. Villeneuve (2010), Global estimates of ambient fine particulate matter concentrations from satellite-based aerosol optical depth: Development and application. Environ. *Health Perspect.*, 118, 847-855, doi: 10.1289/ehp.0901623.

Vecchi, R., G. Marcazzan, G. Valli, M. Ceriani, and C. Antoniazzi (2004), The role of atmospheric dispersion in the seasonal variation of PM1 and PM2.5 concentration and composition in the urban area of Milan (Italy), *Atmos. Environ.*, 38(27), 4437-4446, doi:10.1016/j.atmosenv.2004.05.029.

Wang, F., D. S. Chen, S. Y. Cheng, J. B. Li, M. J. Li, and Z. H. Ren (2010), Identification of regional atmospheric PM10 transport pathways using HYSPLIT, MM5-CMAQ and synoptic pressure pattern analysis, *Environ. Modell. Softw.*, 25, 927-934, doi:10.1016/j.envsoft.2010.02.004.

Wang, J., S. Wang, J. Jiang, A. Ding, M. Zheng, B. Zhao, D. C Wong, W. Zhou, G. Zheng, L. Wang, J. E. Pleim, and J. Hao (2014a), Impact of aerosol–meteorology interactions on fine particle pollution during China's severe haze episode in January 2013, *Environ. Res. Lett.*, 9 094002, doi:10.1088/1748-9326/9/9/09400

Wang, J., J. Feng, Z. Yan, Y. Hu, G. Jia (2012), Nested high-resolution modeling of the impact of urbanization on regional climate in three vast urban agglomerations in China, *J. Geophys. Res. Atmos.*, 117(D21), doi: 10.1029/2012JD018226.

Wang, M., X. Zhang, and X. Yan (2013), Modeling the climatic effects of urbanization in the Beijing-Tianjin-Hebei metropolitan area, *Theor. Appl. Climatol.*, 113, 377-385, doi: 10.1007/s00704-012-0790-z.

Wang, S., J. Wang, Z. Zhou, and K. Shang (2005), Regional characteristics of three kinds of dust storm events in China, *Atmos. Environ.*, 39, 509–520, doi: 10.1016/j.atmosenv.2004.09.033.

Wang, Y., L. Yao, L. Wang, Z. Liu, D. Ji, G. Tang, J. Zhang, Y. Sun, B. Hu, and J. Xin (2014b), Mechanism for the formation of the January 2013 heavy haze pollution episode over central and eastern China, *Sci. China: Earth Sci.*, 51(1), 14-25, doi: 10.1007/s11430-013-4773-4.

Wang, Y., Y. Zhang, J. Hao, and M. Luo (2011), Seasonal and spatial variability of surface ozone over China: contributions from background and domestic pollution, *Atmos. Chem. Phys.*, 11, 3511–3525, doi:10.5194/acp-11-3511-2011.

Whiteman, C. D., X. Bian, and S. Zhong (1999), Wintertime Evolution of the Temperature Inversion in the Colorado Plateau Basin, *J. Appl. Meteor.*, 38, 1103–1117, doi: http://dx.doi.org/10.1175/1520-0450(1999)038<1103:WEOTTI>2.0.CO;2

Wood, R., I. M. Stromberg, and P. R. Jonas (1999), Aircraft observations of sea-breeze frontal structure, *Q. J. Roy. Meteor. Soc.*, 125(558), 1959-1995, doi: 10.1002/qj.49712555804.

Wu, J. B., K. C. Chow, J. C. H. Fung, A. K. H. Lau, and T. Yao (2011), Urban heat island effects of the Pearl River Delta city clusters – their interactions and seasonal variation, *Theor. Appl. Climatol.*, 103, 489-499, doi: 10.1007/s00704-010-0323-6.

Wu, M., D. Wu, Q. Fan, B. M. Wang, H. W. Li, and S. J. Fan (2013), Observational studies of the meteorological characteristics associated with poor air quality over the Pearl River Delta in China, *Atmos. Chem. Phys.*, 13, 10755-10766, doi:10.5194/acp-13-10755-2013.

Wu, Z., M. Hu, P. Lin, S. Liu, B. Wehner, and A. Wiedensohler (2008), Particle numer size distribution in the urban atmosphere of Beijing, China, *Atmos. Environ.*, 42(34), 7967-7980, doi:10.1016/j.atmosenv.2008.06.022.

Xie, S., T. Yu, Y. Zhang., L. Zeng, L. Qi, and X. Tang (2005), Characteristics of PM10, SO2, NOx and O3 in ambient air during the dust storm period in Beijing, *Sci. Total*

Environ., 345(1-3), 153-164, doi:10.1016/j.scitotenv.2004.10.013.

Xu, J., Y. H. Zhang, J. S. Fu, S. Q. Zheng, and W. Wang (2008), Process analysis of typical summertime ozone episodes over the Beijing area, *Sci. Total Environ.*, 399, 147–157, doi:10.1016/j.scitotenv.2008.02.013.

Xu, W. Y., C. S. Zhao, L. Ran, Z. Z. Deng, P. F. Liu, N. Ma, W. L. Lin, X. B. Xu, P. Yan, X. He, J. Yu, W. D. Liang, and L. L. Chen (2011), Characteristics of pollutants and their correlation to meteorological conditions at a suburban site in the North China Plain, *Atmos. Chem. Phys.*, 11, 4353–69, doi:10.5194/acp-11-4353-2011.

Yamaji, K., T. Ohara, I. Uno, H. Tanimoto, J. Kurokawa, and H. Akimoto (2006), Analysis of the seasonal variation of ozone in the boundary layer in East Asia using the Community Multi-scale Air Quality model: What controls surface ozone levels over Japan?, *Atmos. Environ.*, 40(10), 1856–1868, doi:10.1016/j.atmosenv.2005.10.067.

Yang, P., G. Ren, and W. Liu (2013), Spatial and Temporal Characteristics of Beijing Urban Heat Island Intensity, *J. Appl. Meteor. Clim.*, 52(8), 1803–1816, doi:10.1175/JAMC-D-12-0125.1.

Zhang, H., Y. Wang, J. Hu, Q. Ying, and X.-M. Hu (2015a), Relationships between meteorological parameters and criteria air pollutants in three megacities in China, *Environ. Res.,* 140, 242–254, doi:10.1016/j.envres.2015.04.004.

Zhang, Q., D. G. Streets, G. R. Carmichael, K. B. He, H. Huo, A. Kannari, Z. Klimont, I. S. Park, S. Reddy, J. S. Fu, D. Chen, L. Duan, Y. Lei, L. T. Wang, and Z. L. Yao

(2009), Asian emissions in 2006 for the NASA INTEX-B mission, *Atmos. Chem. Phys.*, 9(14), 5131–5153, doi:10.5194/acp-9-5131-2009.

Zhang, R., J. Jing, J. Tao, S. C. Hsu, G. Wang, J. Cao, C. S. L. Lee, L. Zhu, Z. Chen, Y. Zhao, and Z. Shen (2013), Chemical characterization and sources apportionment of PM2.5 in Beijing: seasonal perspective, *Atmos. Chem. Phys.,* 13(4), 7053-7074, doi:10.5194/acp-13-7053-2013.

Zhang, Y., S. Miao, Y. Dai, and Y. Liu (2013), Numerical simulation of characteristics of summer clear day boundary layer in Beijing and the impact of urban underlying surface on sea breeze, *CHINESE J. Geophys. Ed.*, 8(56), 2558–2573, doi:10.6038/cjg20130806.

Zhang, Z., X. Zhang, D. Gong, W. Quan, X. Zhao, Z. Ma, and S. J. Kim (2015b), Evolution of surface O3 and PM2.5 concentrations and their relationships with meteorological conditions over the last decade in Beijing, *Atmos. Environ.*, doi: 10.1016/j.atmosenv.2015.02.071.

Zhao, X., X. Zhang, X. Xu, J. Xu, W. Meng, and W. Pu (2009), Seasonal and diurnal variation of ambient PM2.5 concentration in urban and rural environments in Beijing, *Atmos. Environ.*, 43(18), 2893-2900, doi:10.1016/j.atmosenv.2009.03.009.

Zhao, X., G. Zhuang, Z. Wang, Y. Sun, Y. Wang, and H. Yuan (2007), Variation of sources and mixing mechanism of mineral dust with pollution aerosol – revealed by the two peaks of a super dust storm in Beijing, *Atmos. Res.*, 84(3), 265-279, doi:10.1016/j.atmosres.2006.08.005.

Figure captions

Figure 1. (a) Map of model domains and terrain height (km), (b) tracer (SO2) emission [Zhang et al., 2009] in domain 1, and (c) land use categories in domain 3. The locations of observation sites from the National Climatic Data Center (NCDC) data are indicated by black dots in (a). The black line in (c) indicates the location of vertical cross sections shown in Figures 6, 7, 11, 12, 14, 16, 17, 19, which crosses Beijing (BJ), Langfang (LF) and Tianjin (TJ). The location of BTH region is marked by red solid lines in (a) and (b).

Figure 2. The seasonally averaged geopotential height (GH) fields overlaid by the wind vectors at 850-hPa in domain 1 in (a) Spring, (b) Summer, (c) Fall, and (d) Winter. The seasonally averaged geopotential height fields are derived by averaging all the NCEP FNL analysis (includes 4 times a day) in each season of 2010. The location of BTH region is marked by the red solid lines.

Figure 3. Spatial distribution of 2-m temperature fields (K) over land at 1400 LT in (a) Spring, (b) Summer, (c) Fall, and (d) Winter in domain 1 simulated by the four idealized simulations. Seasonal mean observations from the NCDC data are overlaid using colored circles.

Figure 4. Similar as Figure 3, but for the 2-m relative humidity (RH) fields at 1400 LT in (a) spring, (b) summer, (c) fall, and (d) winter.

Figure 5. Spatial distribution of simulated (a-d) wind speed (WS), (e-h) vertical velocity (w), (i-l) relative humidity (RH), and (m-p) potential temperature (PT) fields at ~125 m AGL, overlaid with 10-m wind vector at (top to bottom) 1200 LT, 1500 LT,

1700 LT, and 2000 LT in fall. The black line in (e-h) indicates the locations of vertical cross sections shown in Figures 6, 7, 11, 12, 14, 16, 17, 19.

Figure 6. Vertical cross sections of simulated wind field at (a) 1200 LT, (b) 1500 LT, (c) 1700 LT, and (d) 2000 LT in fall. The location of the cross section is marked in Figure 4e. The color shape represents the vertical velocity (w). The pink dashed line represents the top of BL. Note that the vertical velocity is multiplied by a factor of 20 when plotting wind vectors. The locations of sea and urban areas are indicated by the blue and red lines, respectively.

Figure 7. Similar as Figure 6, but for the vertical cross sections of potential temperature (PT) in fall. The three black lines in (b) indicate the locations where the potential temperature profiles shown in Figure 8 are extracted.

Figure 8. The potential temperature (PT) profiles at 1500 LT over Beijing (BJ), Tianjin (TJ) and Langfang (LF) in (a) Spring, (b) Summer, (c) Fall, and (d) Winter. The locations of the three sites are indicated in Figure 7b by the black lines.

Figure 9. The distribution of BLH (m) at 1500 LT in (a) Spring, (b) Summer, (c) Fall, and (d) Winter. The two dashed lines in (c) indicate the zone with relatively low BLH in fall.

Figure 10. The distributions of simulated tracer (SO_2) at the lowest vertical layer (~10 m AGL), overlaid with 10-m wind vector fields at 1500 LT in (a) spring, (b) summer, (c) fall, and (d) winter.

Figure 11. The vertical cross sections of tracer (SO_2) at 1500 LT in (a) spring, (b) summer, (c) fall, and (d) winter. Note that the vertical velocity is multiplied by a

factor of 20 when plotting wind vectors.

Figure 12. The vertical cross sections of potential temperature (PT) at (a) 0000 LT, (b) 0400 LT, (c) 0600 LT and (d) 1000 LT in fall. Note that the vertical velocity is multiplied by a factor of 20 when plotting wind vectors.

Figure 13. Spatial distribution of simulated (a-d) vertical velocity (w), and (e-h) relative humidity (RH) at ~125 m AGL, overlaid with 10-m wind vector at (top to bottom) 1200 LT, 1500 LT, 1700 LT, and 2000 LT in winter.

Figure 14. The vertical cross sections of potential temperature (PT) at (a) 1200 LT, (b) 1500 LT, (c) 1700 LT, and (d) 2000 LT in winter. Note that the vertical velocity is multiplied by a factor of 20 when plotting wind vectors..

Figure 15. Similar as Figure 13, but for summer.

Figure 16. The vertical cross sections of potential temperature (PT) at (a) 1200 LT, (b) 1500 LT, (c) 1700 LT, and (d) 2000 LT in summer. Note that the vertical velocity is multiplied by a factor of 20 when plotting wind vectors.

Figure 17. The vertical cross sections of horizontal wind speed (WS) at (a-d) 0600 LT and (e-h) 1500 LT in (left to right) spring, summer, fall, and winter. Note that the vertical velocity is multiplied by a factor of 20 when plotting wind vectors.

Figure 18. Similar as Figure 13, but for spring.

Figure 19. The vertical cross sections of potential temperature (PT) at (a) 1200 LT, (b) 1500 LT, (c) 1700 LT, and (d) 2000 LT in spring. Note that the vertical velocity is multiplied by a factor of 20 when plotting wind vectors.

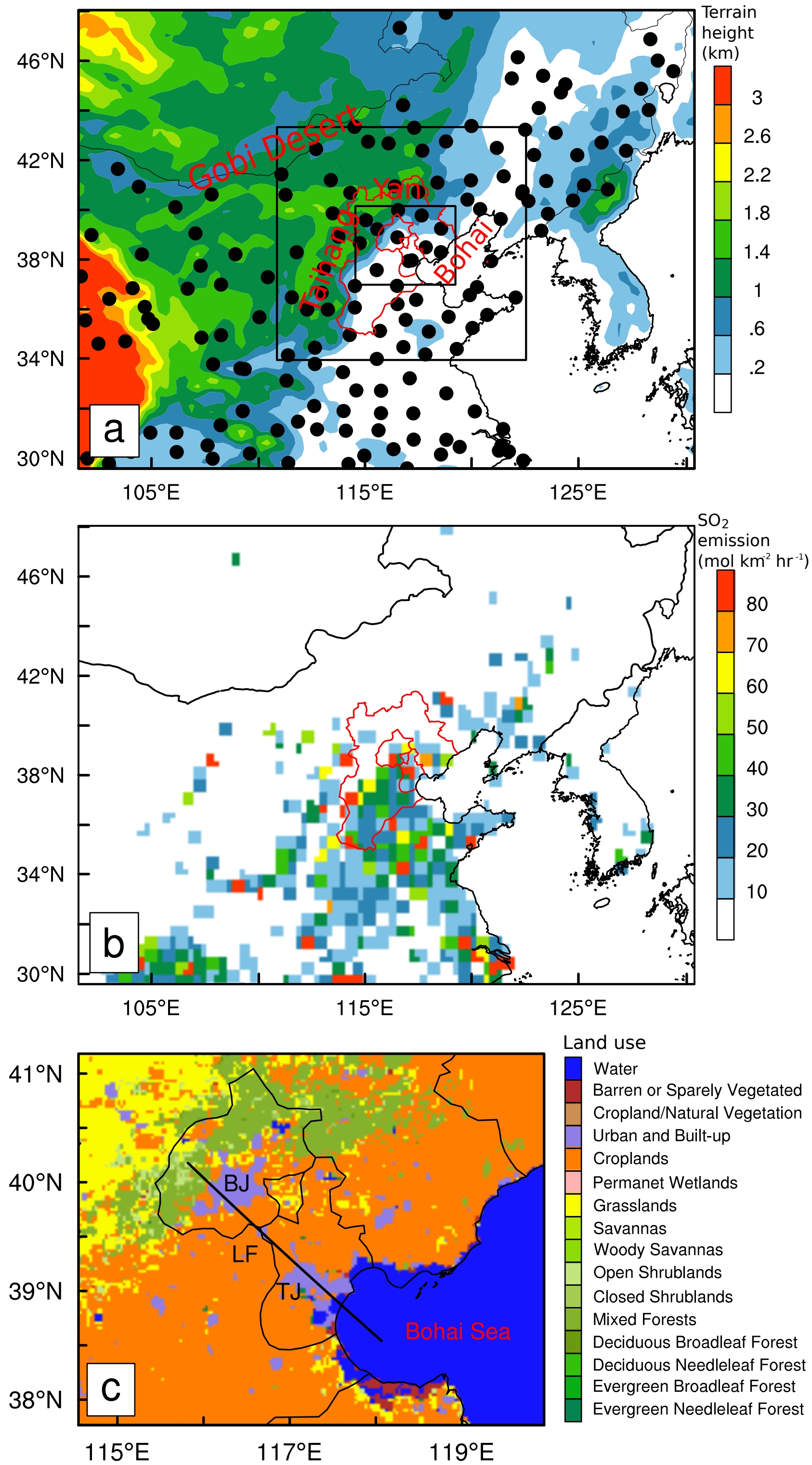

Terrain height (km)
3
2.6
2.2
1.8
1.4
1
.6
.2
Gobi Desert
Taihang
Yan
Bohai
46°N
42°N
38°N
34°N
30°N
105°E
115°E
125°E
a
SO2 emission (mol km² hr⁻¹)
80
70
60
50
40
30
20
10
b
Land use
Water
Barren or Sparely Vegetated
Cropland/Natural Vegetation
Urban and Built-up
Croplands
Permanet Wetlands
Grasslands
Savannas
Woody Savannas
Open Shrublands
Closed Shrublands
Mixed Forests
Deciduous Broadleaf Forest
Deciduous Needleleaf Forest
Evergreen Broadleaf Forest
Evergreen Needleleaf Forest
BJ
LF
TJ
Bohai Sea
41°N
40°N
39°N
38°N
115°E
117°E
119°E
c

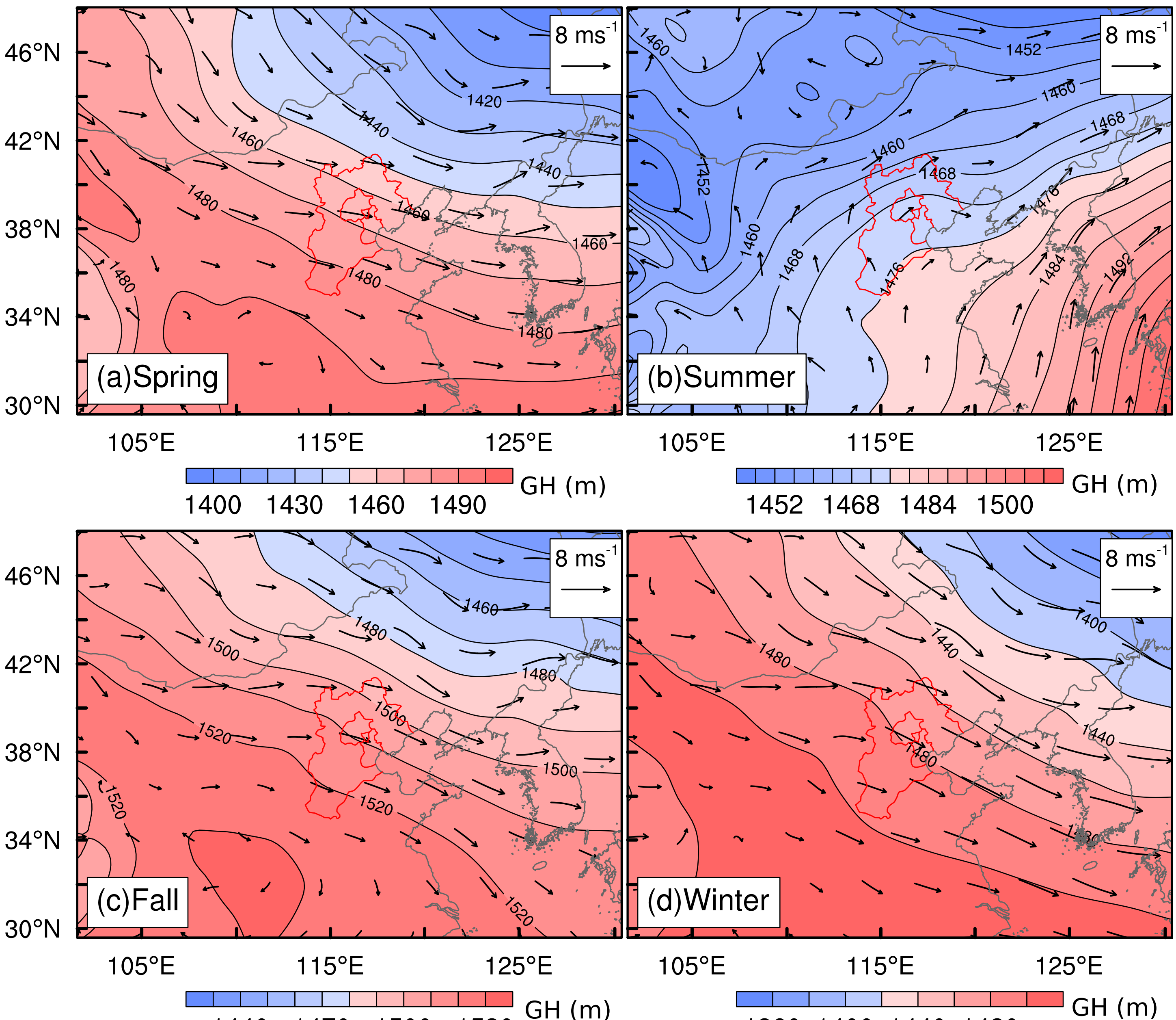

(a)Spring
(b)Summer
(c)Fall
(d)Winter
8 ms-1
GH (m)
1400 1430 1460 1490
1452 1468 1484 1500
1440 1470 1500 1530
1360 1400 1440 1480
46°N
42°N
38°N
34°N
30°N
105°E
115°E
125°E

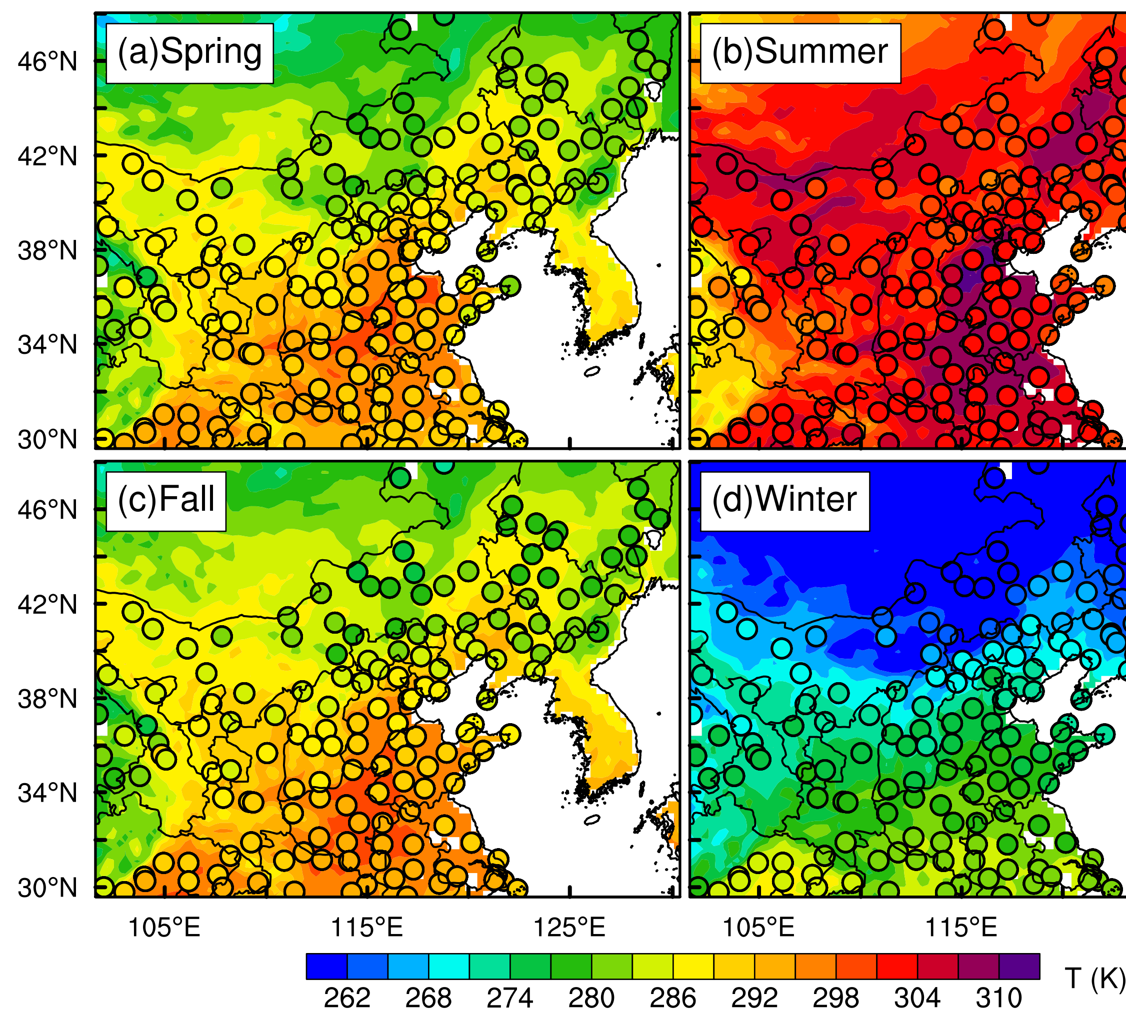

(a)Spring
(b)Summer
(c)Fall
(d)Winter
46°N
42°N
38°N
34°N
30°N
105°E
115°E
125°E
262
268
274
280
286
292
298
304
310
T (K)

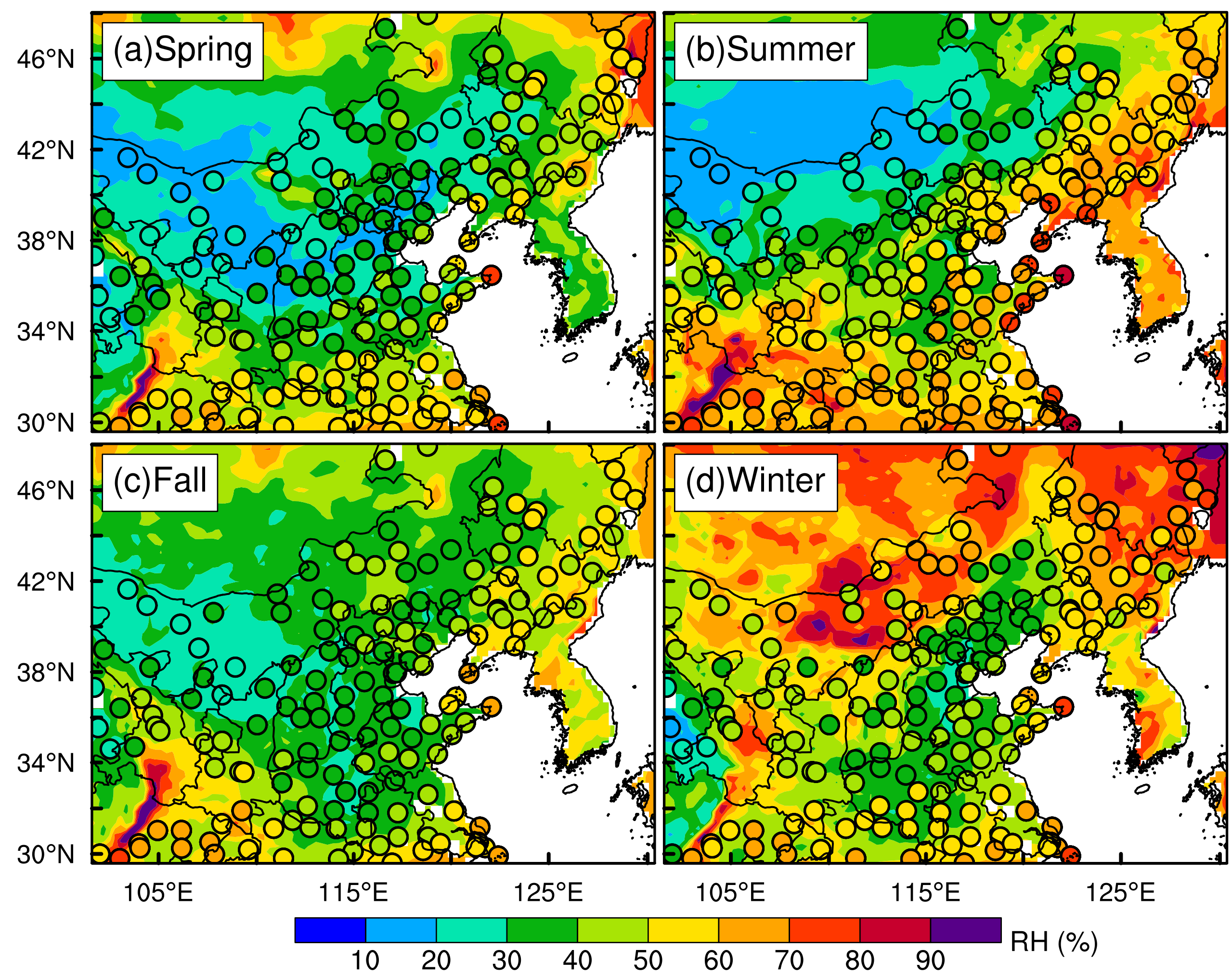

(a)Spring
(b)Summer
(c)Fall
(d)Winter
46°N
42°N
38°N
34°N
30°N
105°E
115°E
125°E
10
20
30
40
50
60
70
80
90
RH (%)

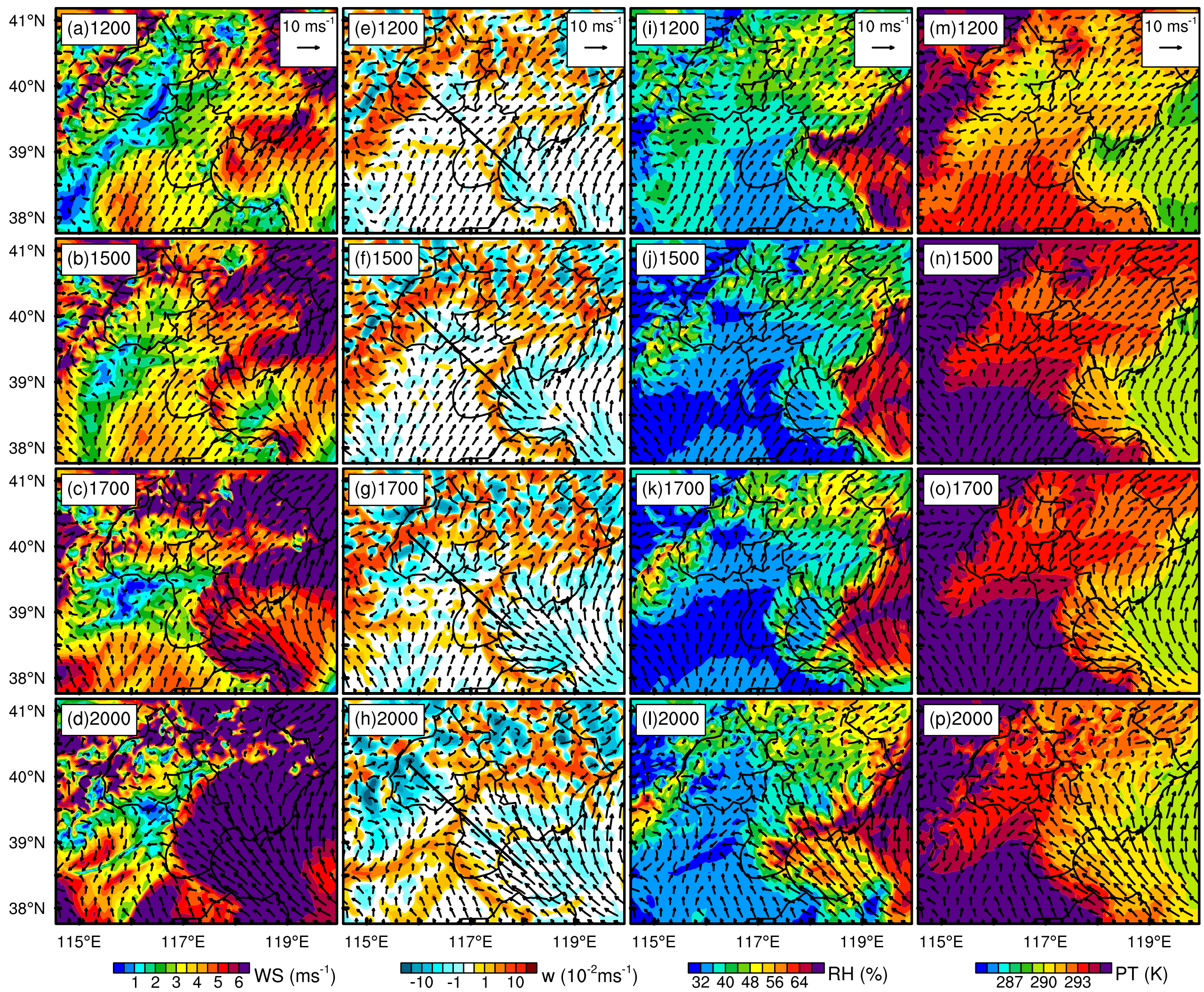

(a)1200
(b)1500
(c)1700
(d)2000
(e)1200
(f)1500
(g)1700
(h)2000
(i)1200
(j)1500
(k)1700
(l)2000
(m)1200
(n)1500
(o)1700
(p)2000
10 ms-1
41°N
40°N
39°N
38°N
115°E
117°E
119°E
1 2 3 4 5 6 WS (ms-1)
-10 -1 1 10 w (10-2ms-1)
32 40 48 56 64 RH (%)
287 290 293 PT (K)

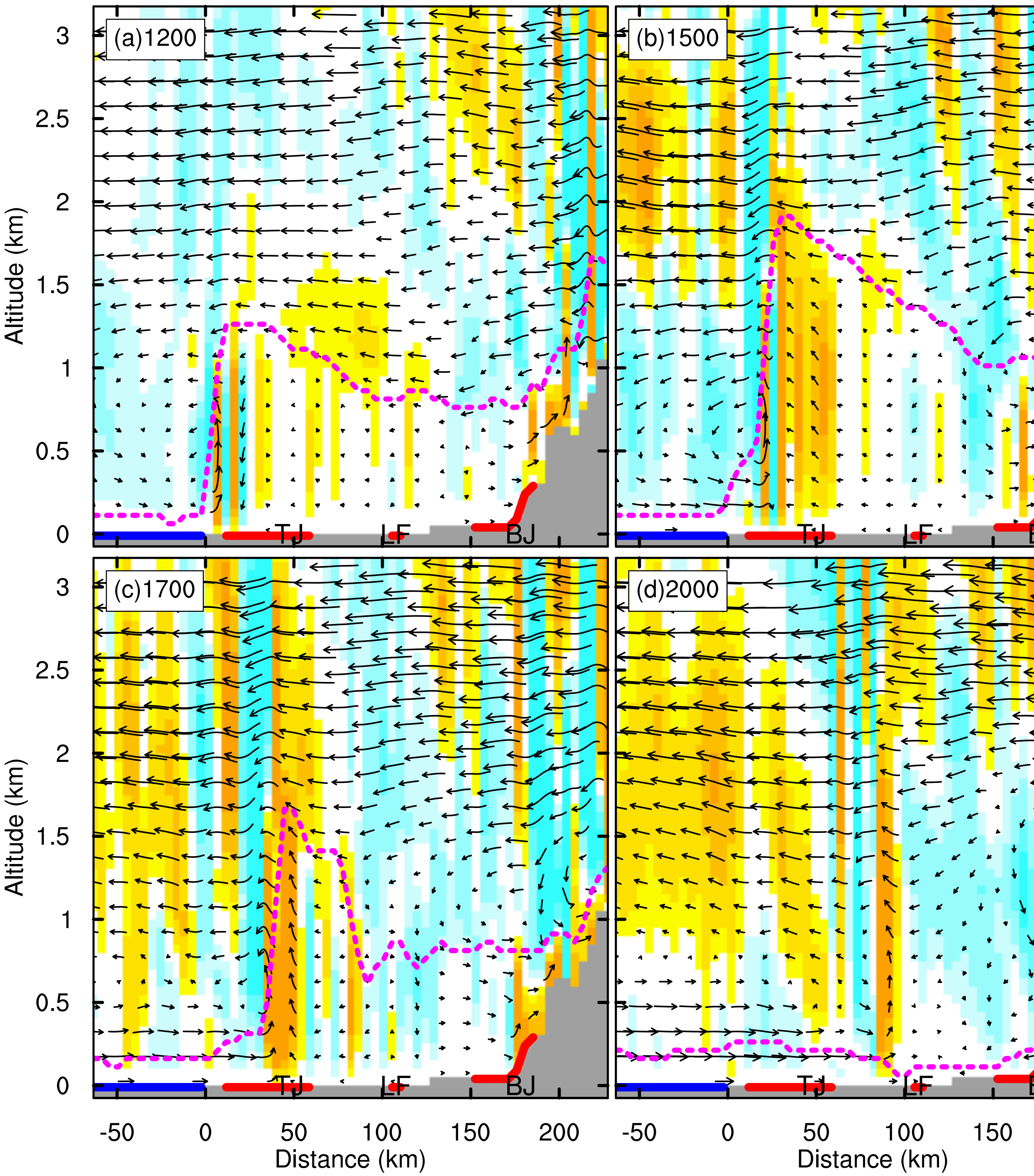

(a)1200
(b)1500
(c)1700
(d)2000
5 ms-1
TJ
LF
BJ
Altitude (km)
Distance (km)
w (ms-1)
-0.09
-0.06
-0.03
0
0.03
0.06
0.09

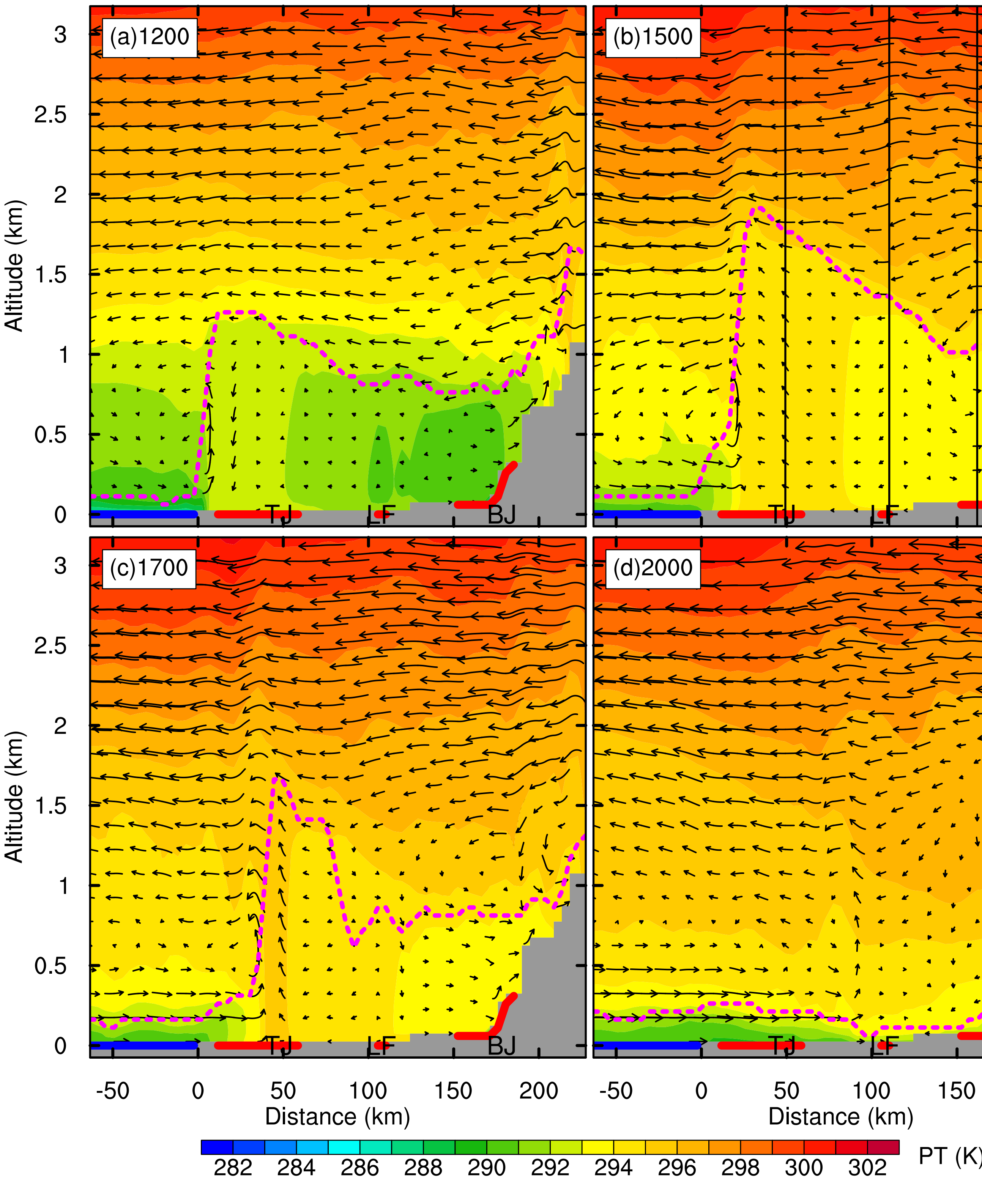

(a)1200
(b)1500
(c)1700
(d)2000
5 ms-1
Altitude (km)
Distance (km)
TJ
LF
BJ
PT (K)
282
284
286
288
290
292
294
296
298
300
302

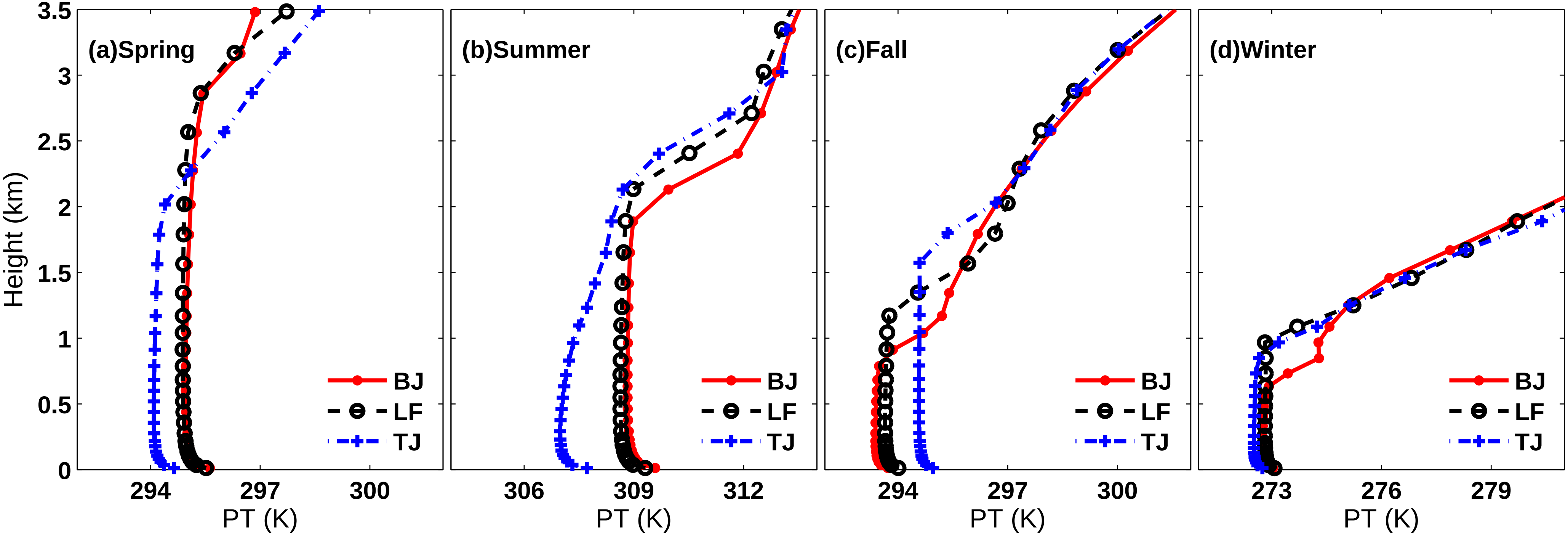

(a)Spring
(b)Summer
(c)Fall
(d)Winter
Height (km)
PT (K)
BJ
LF
TJ
0
0.5
1
1.5
2
2.5
3
3.5
294
297
300
306
309
312
294
297
300
273
276
279

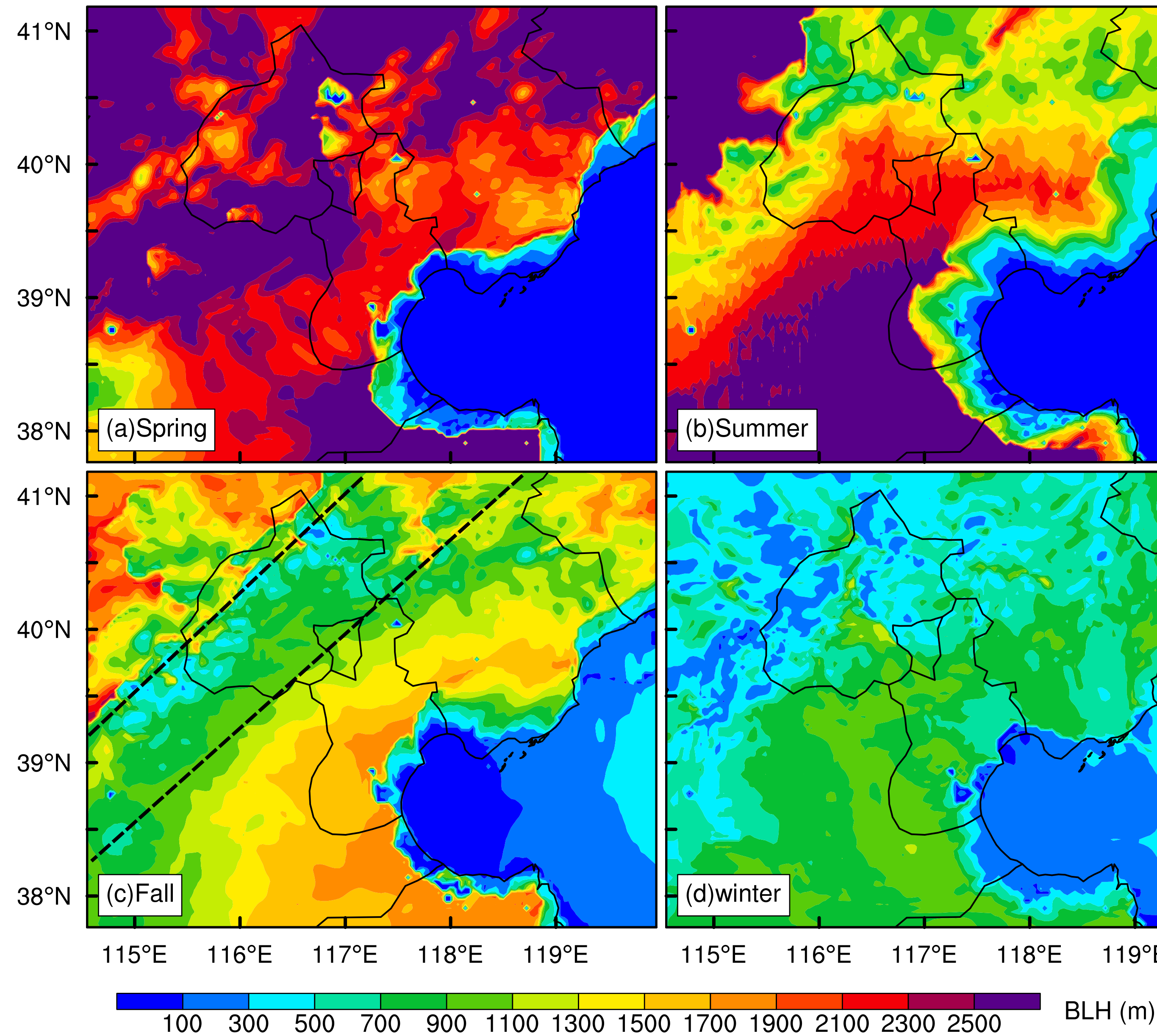

41°N
40°N
39°N
38°N
(a)Spring
(b)Summer
(c)Fall
(d)winter
115°E
116°E
117°E
118°E
119°E
100
300
500
700
900
1100
1300
1500
1700
1900
2100
2300
2500
BLH (m)

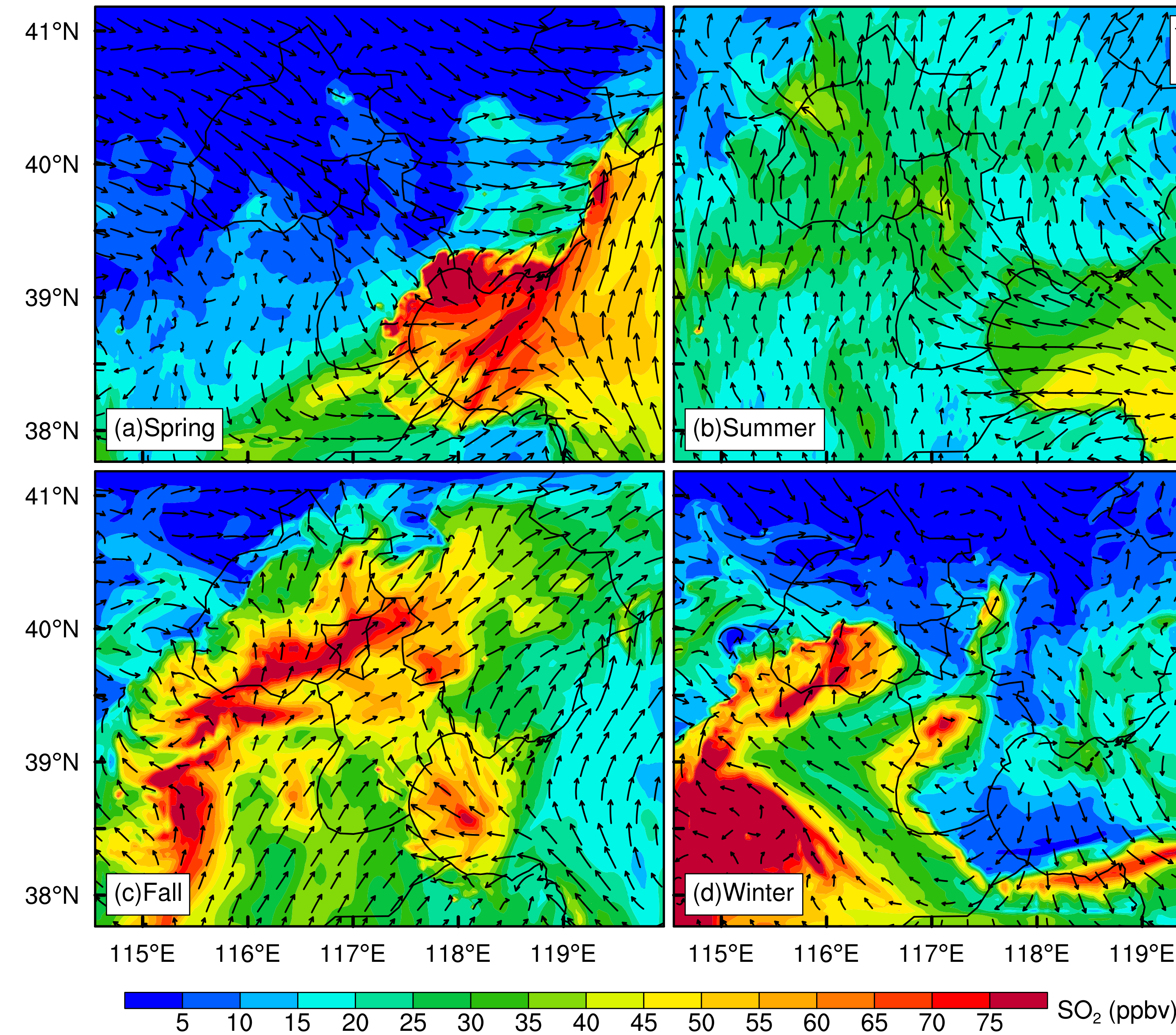

41°N
40°N
39°N
38°N
(a)Spring
(b)Summer
(c)Fall
(d)Winter
10 ms-1
115°E
116°E
117°E
118°E
119°E
5
10
15
20
25
30
35
40
45
50
55
60
65
70
75
SO2 (ppbv)

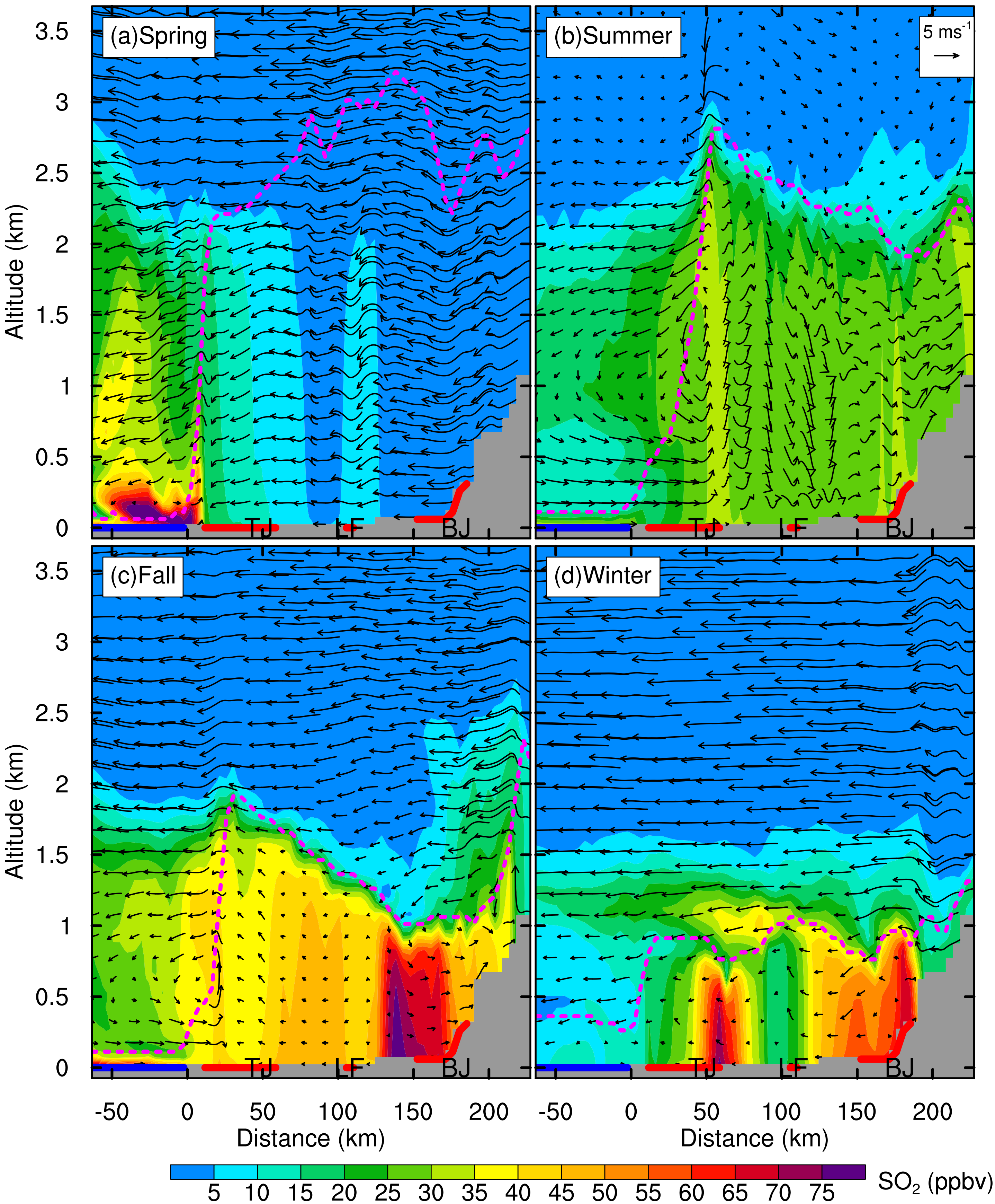

(a)Spring
(b)Summer
(c)Fall
(d)Winter
5 ms-1
Altitude (km)
Distance (km)
TJ
LF
BJ
SO2 (ppbv)
5 10 15 20 25 30 35 40 45 50 55 60 65 70 75

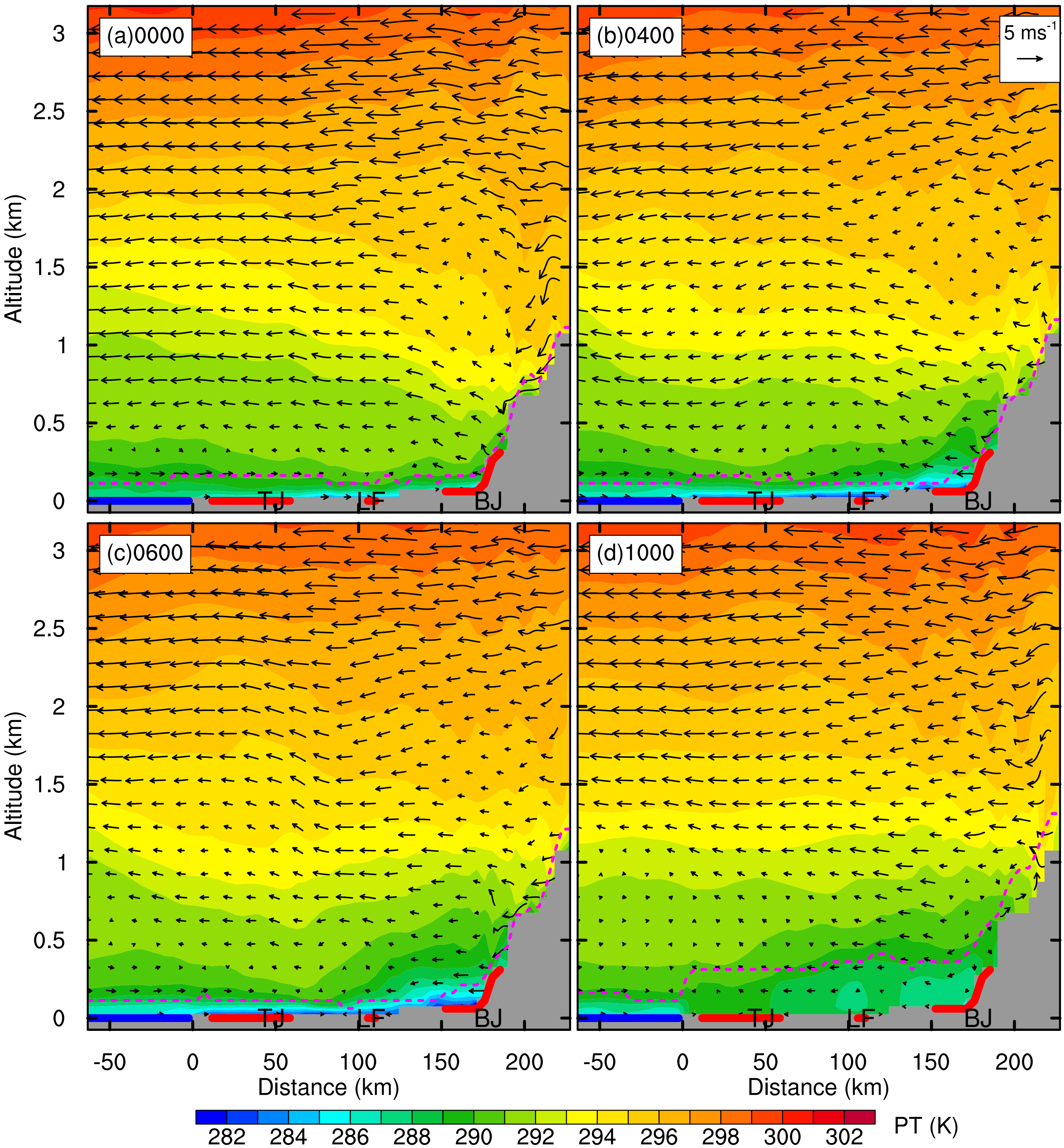

(a)0000
(b)0400
(c)0600
(d)1000
5 ms-1
Altitude (km)
Distance (km)
TJ
LF
BJ
PT (K)
282
284
286
288
290
292
294
296
298
300
302
-50
0
50
100
150
200
0
0.5
1
1.5
2
2.5
3

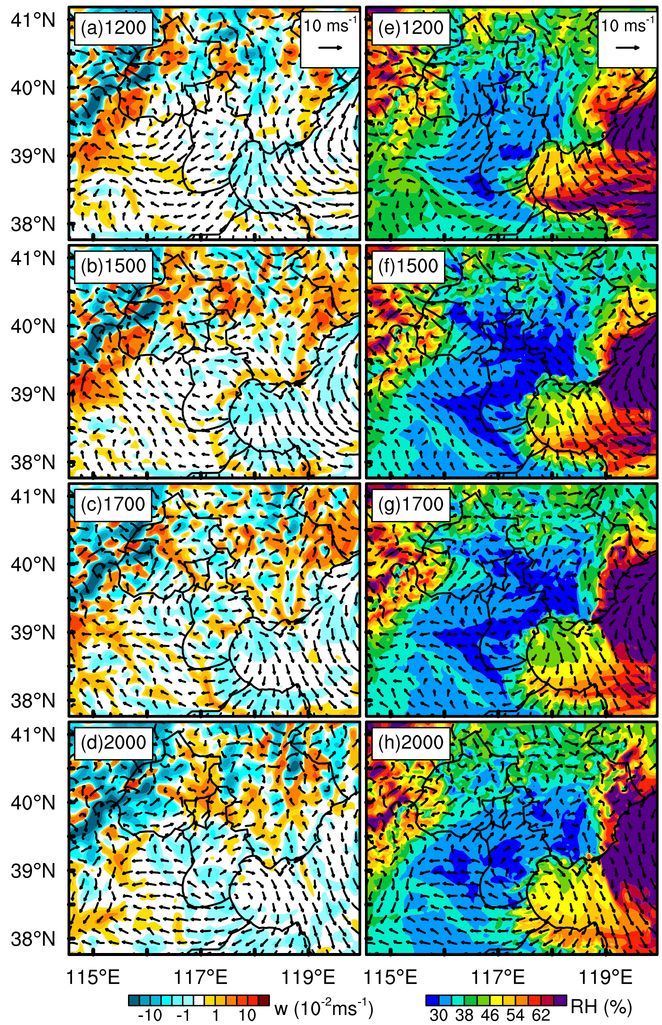

(a)1200
(b)1500
(c)1700
(d)2000
(e)1200
(f)1500
(g)1700
(h)2000
10 ms-1
41°N
40°N
39°N
38°N
115°E
117°E
119°E
-10 -1 1 10 w (10-2ms-1)
30 38 46 54 62 RH (%)

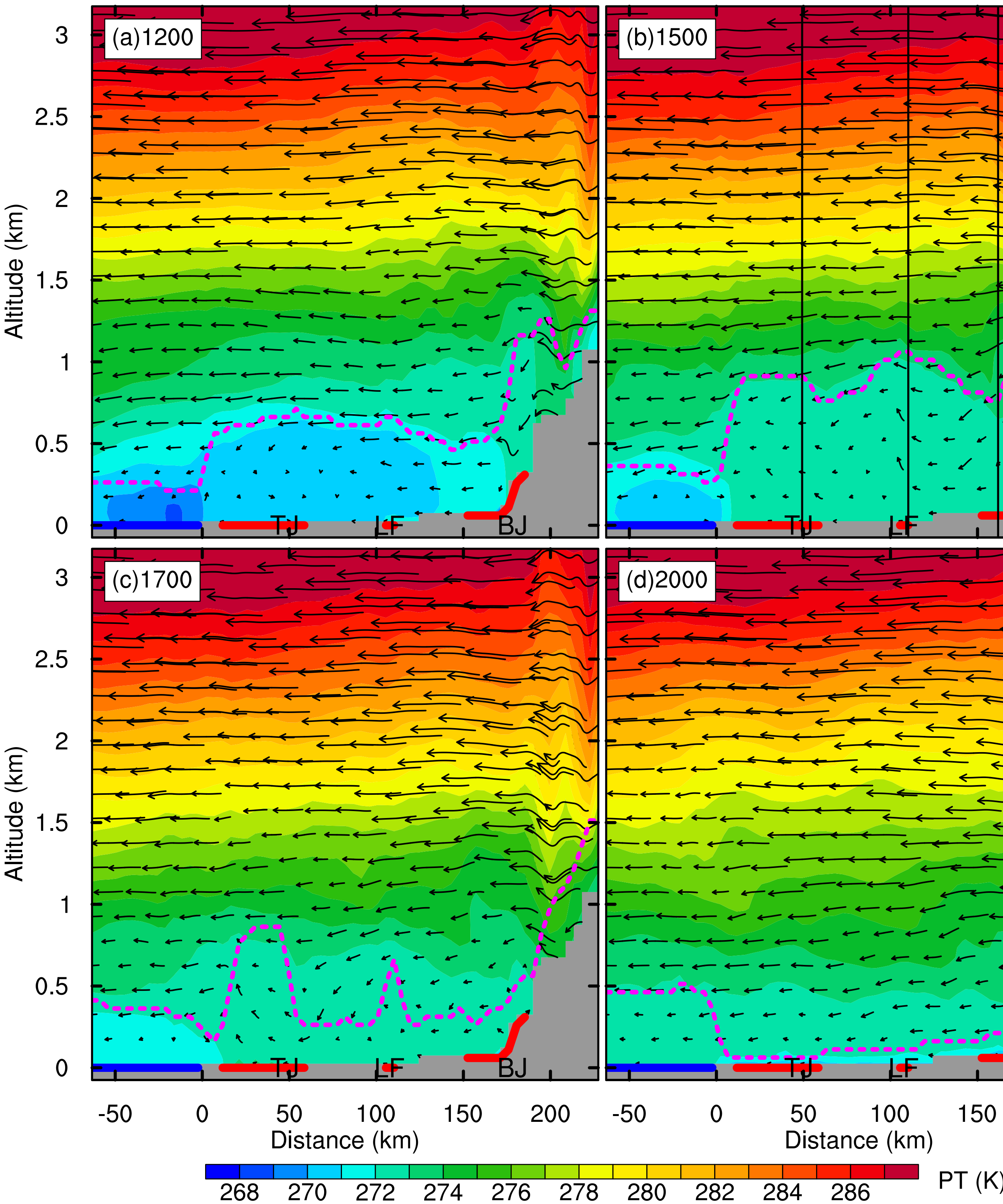

(a)1200
(b)1500
(c)1700
(d)2000
5 ms-1
Altitude (km)
Distance (km)
TJ
LF
BJ
PT (K)
268
270
272
274
276
278
280
282
284
286

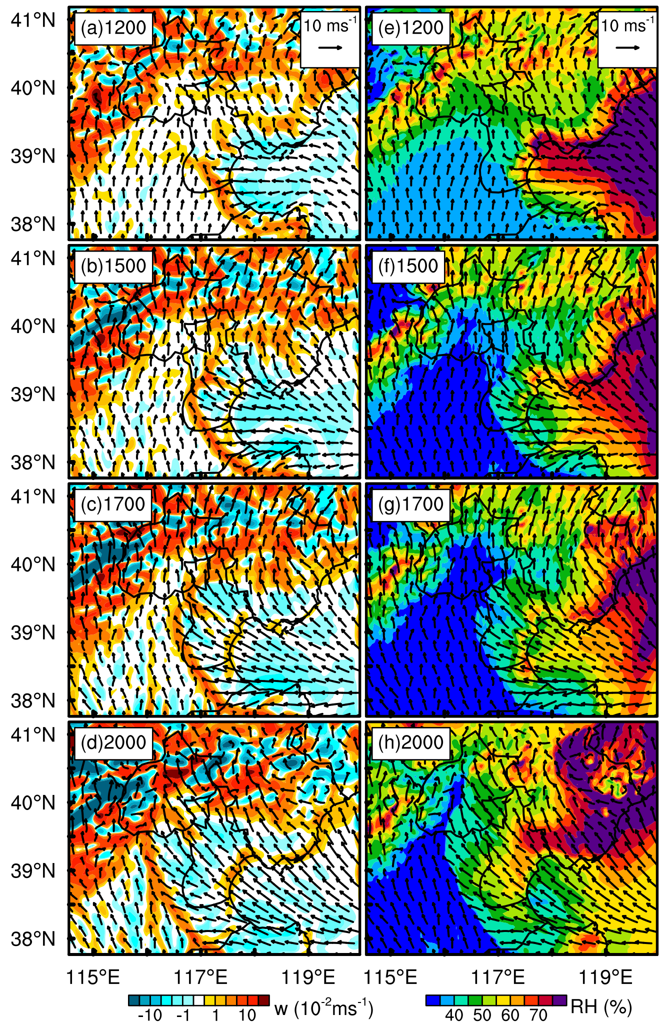

(a)1200
(b)1500
(c)1700
(d)2000
(e)1200
(f)1500
(g)1700
(h)2000
10 ms-1
41°N
40°N
39°N
38°N
115°E
117°E
119°E
-10
-1
1
10
w (10-2ms-1)
40
50
60
70
RH (%)

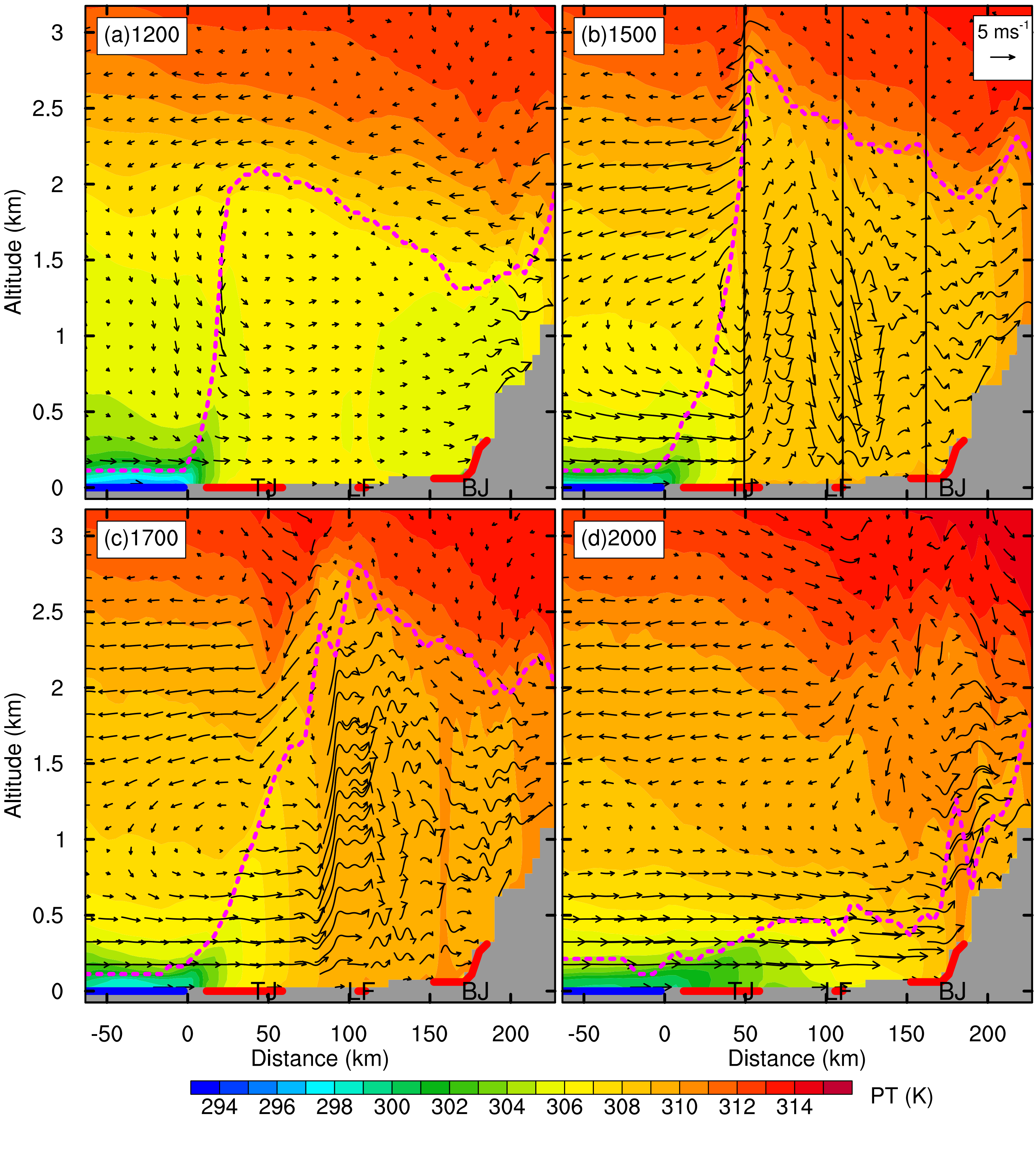
(a)1200
(b)1500
(c)1700
(d)2000
5 ms-1
Altitude (km)
Distance (km)
TJ
LF
BJ
PT (K)
294
296
298
300
302
304
306
308
310
312
314
-50
0
50
100
150
200
0
0.5
1
1.5
2
2.5
3

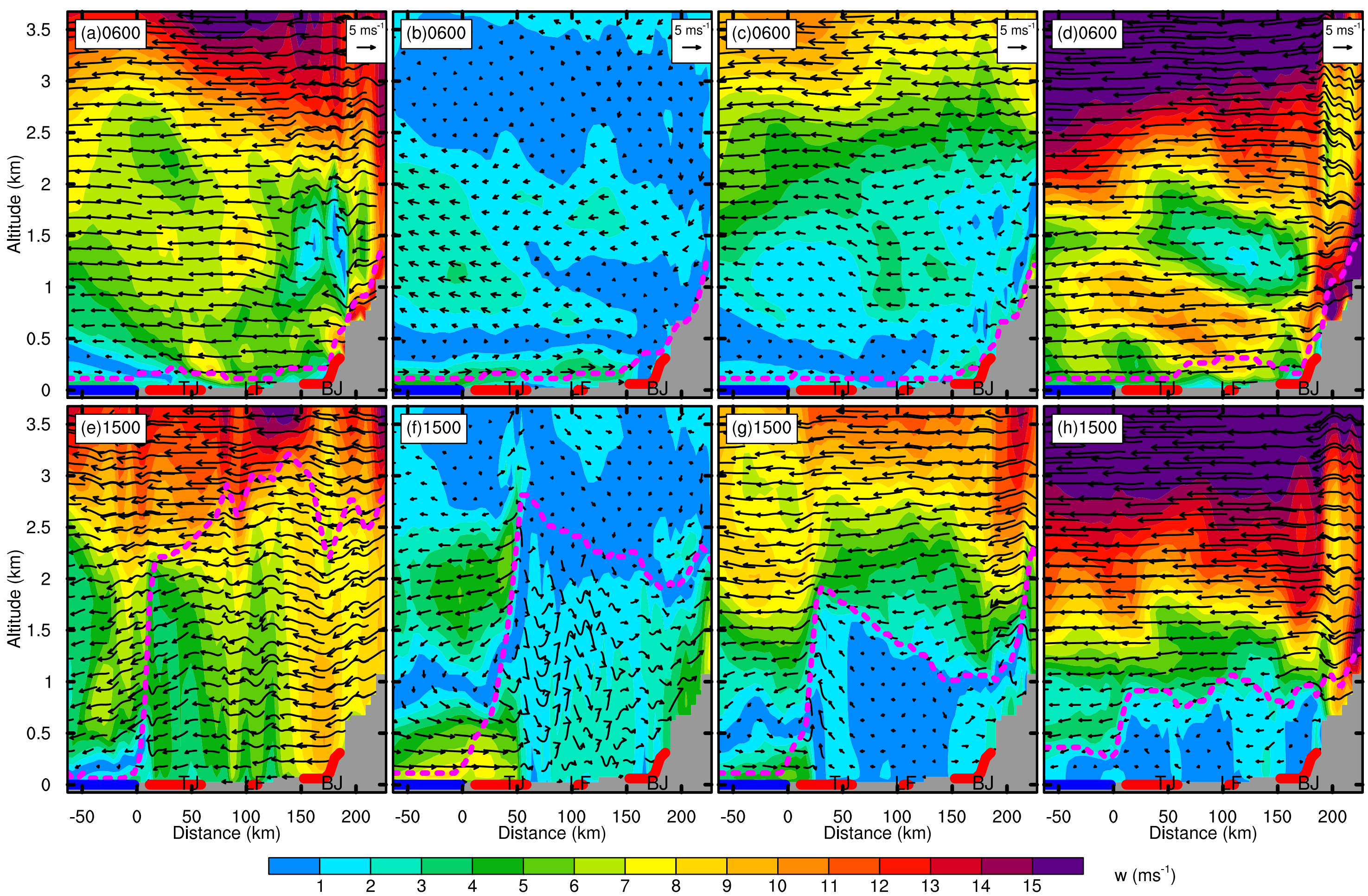

(a)0600
(b)0600
(c)0600
(d)0600
(e)1500
(f)1500
(g)1500
(h)1500
5 ms-1
Altitude (km)
Distance (km)
TJ
LF
BJ
w (ms-1)

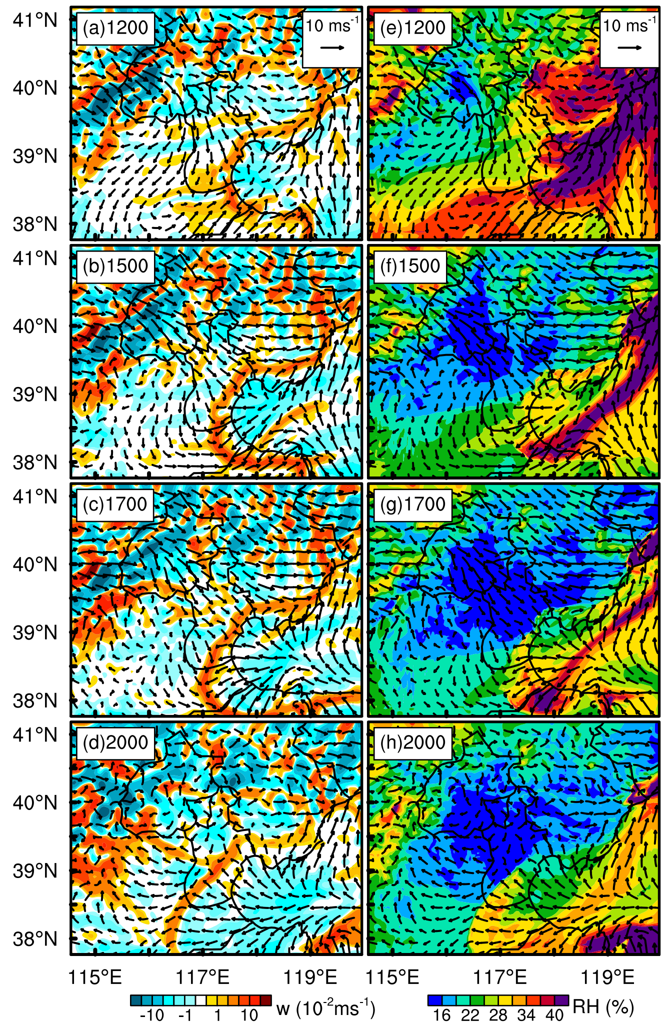

(a)1200
(b)1500
(c)1700
(d)2000
(e)1200
(f)1500
(g)1700
(h)2000
10 ms-1
41°N
40°N
39°N
38°N
115°E
117°E
119°E
-10
-1
1
10
w (10-2ms-1)
16
22
28
34
40
RH (%)

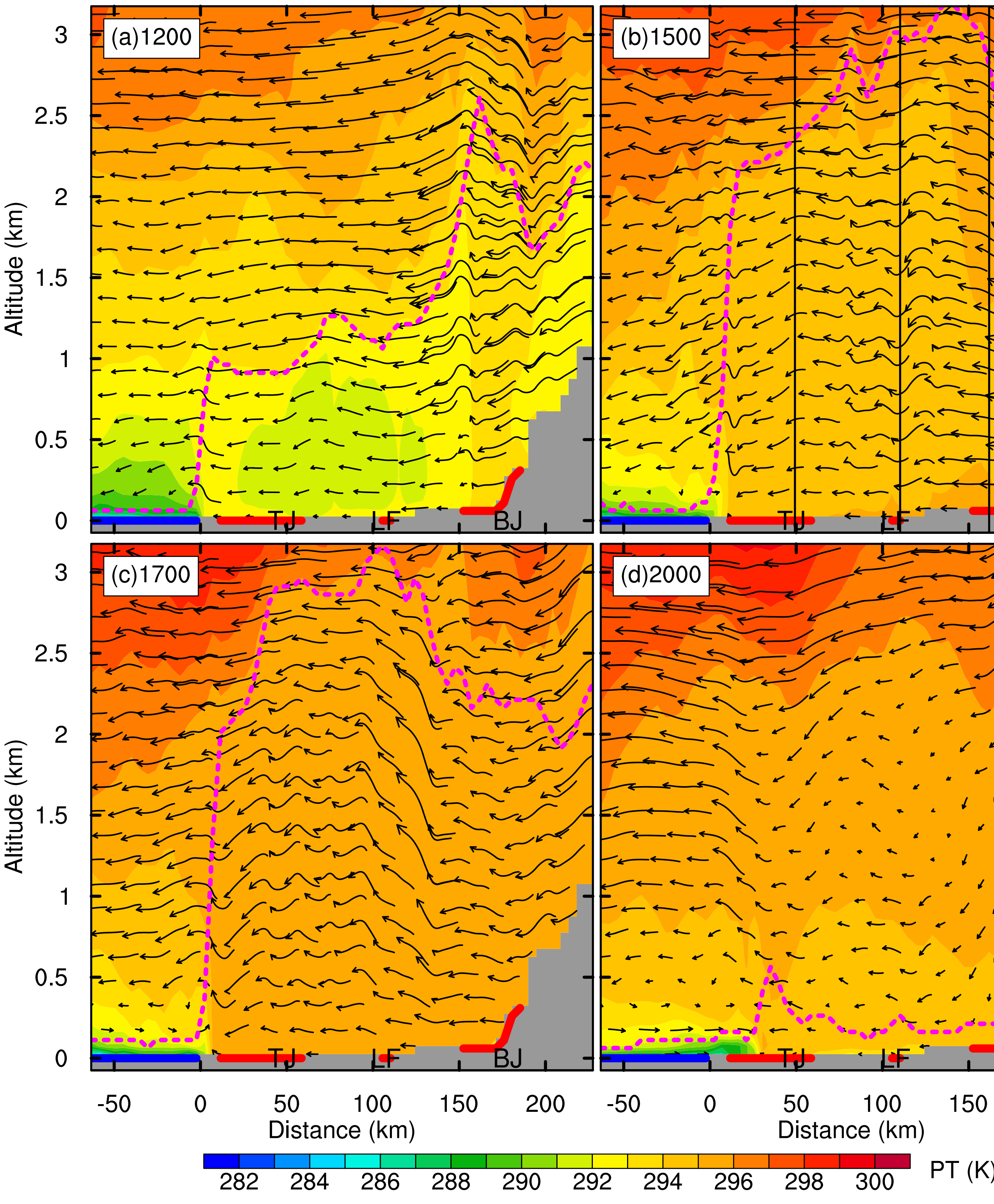
(a)1200
(b)1500
(c)1700
(d)2000
5 ms-1
Altitude (km)
Distance (km)
TJ
LF
BJ
PT (K)
282
284
286
288
290
292
294
296
298
300

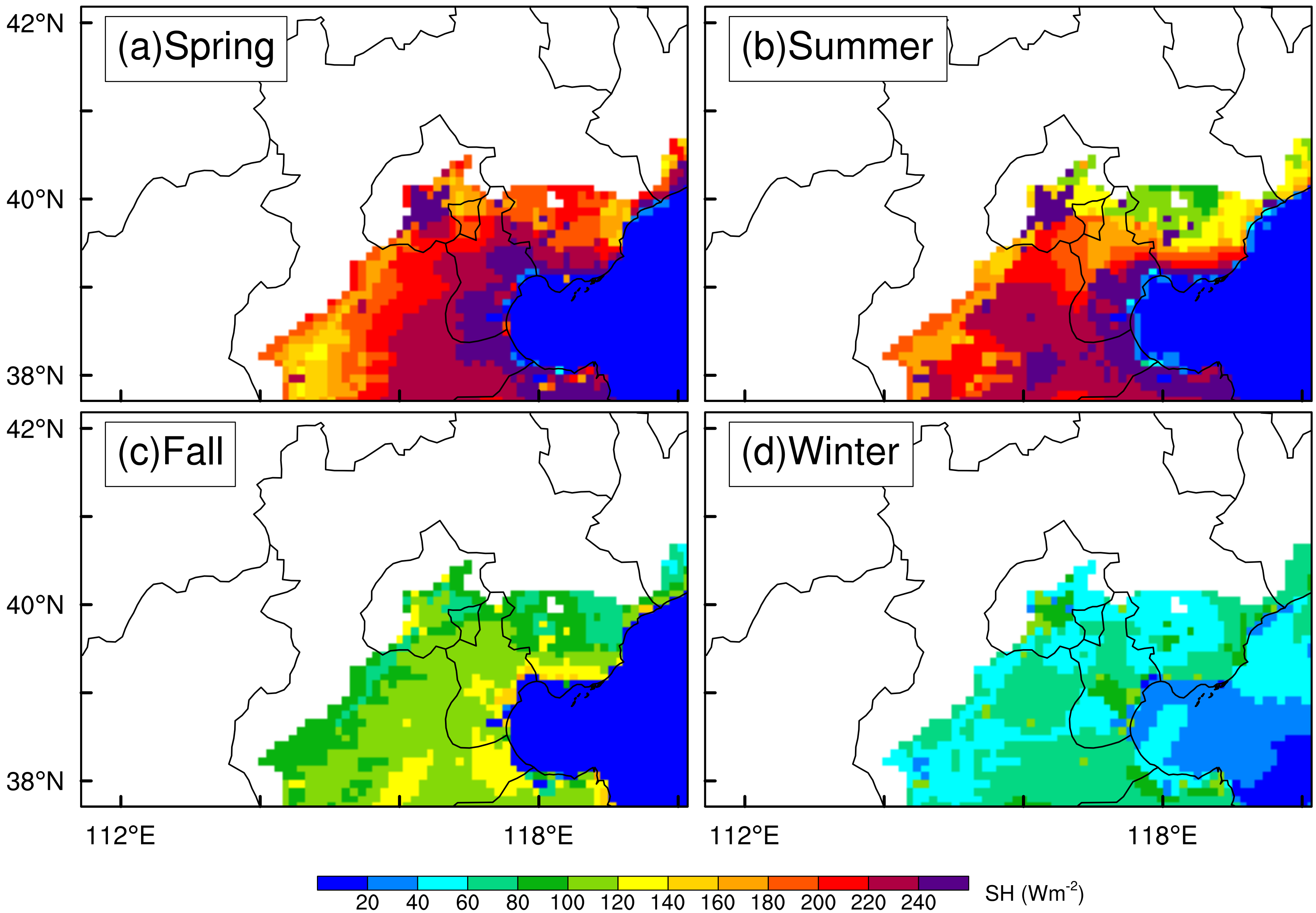
(a)Spring
(b)Summer
(c)Fall
(d)Winter
42°N
40°N
38°N
112°E
118°E
20 40 60 80 100 120 140 160 180 200 220 240
SH (Wm^{-2})

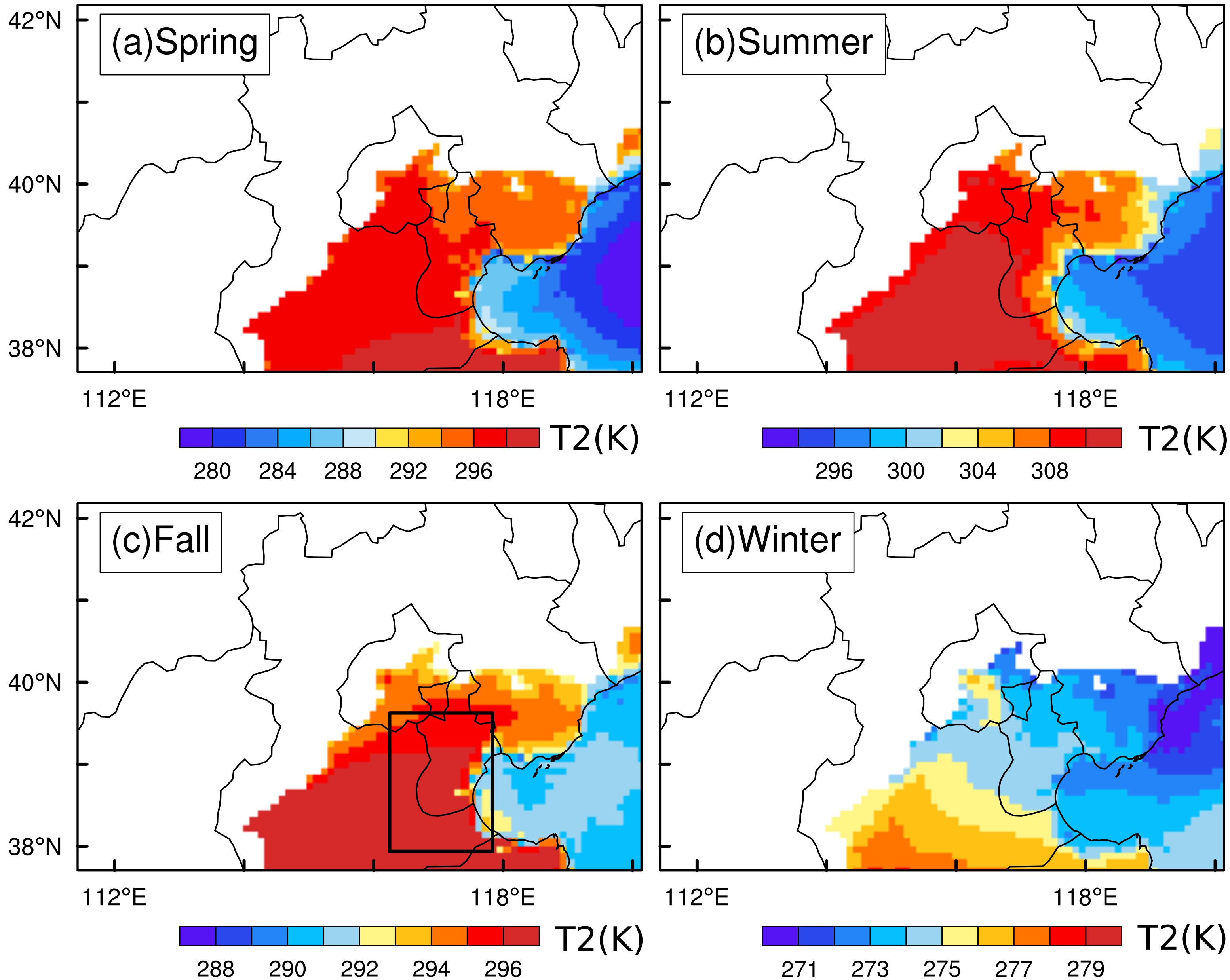

(a)Spring
(b)Summer
(c)Fall
(d)Winter
42°N
40°N
38°N
112°E
118°E
T2(K)
280 284 288 292 296
296 300 304 308
288 290 292 294 296
271 273 275 277 279

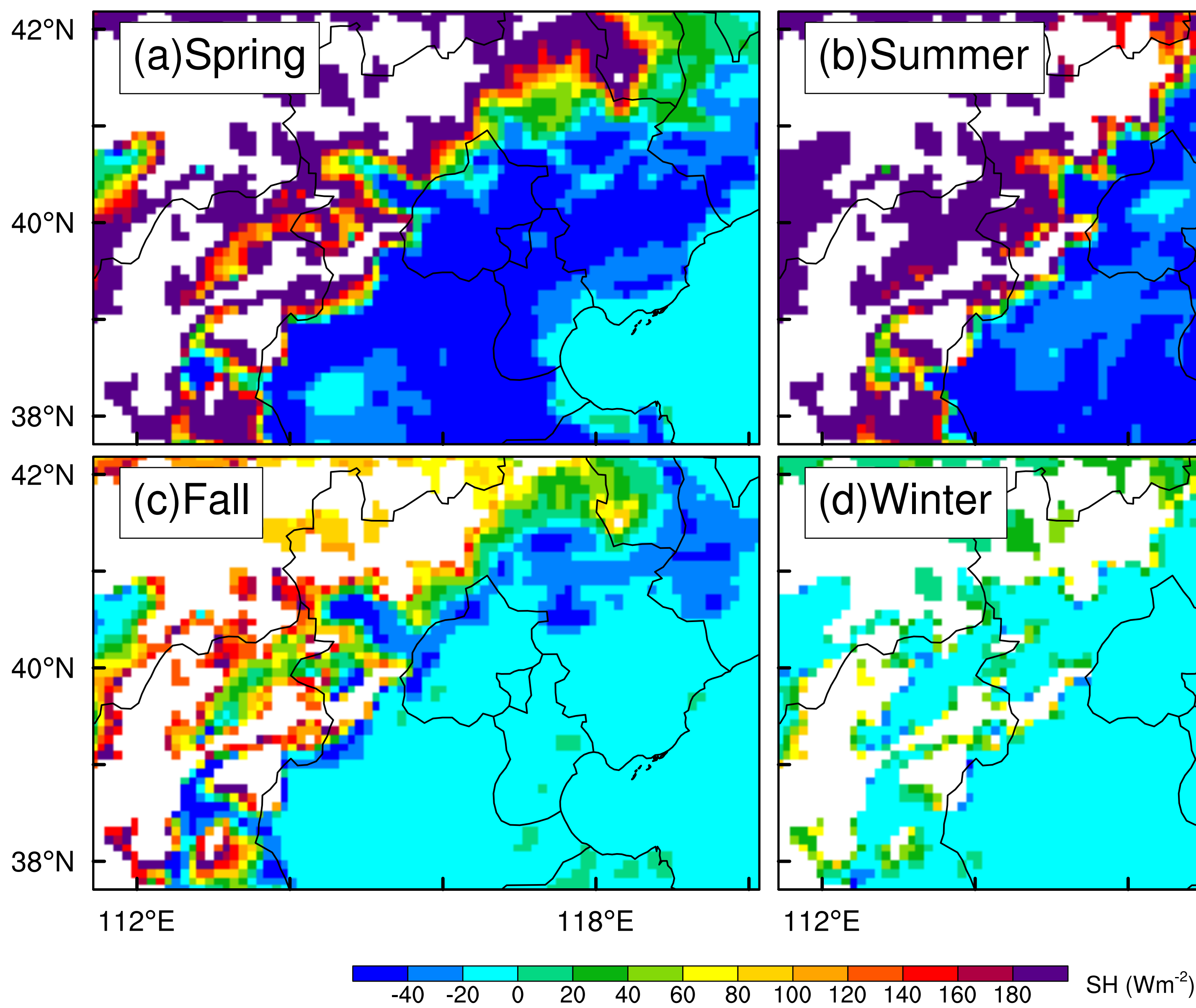
(a)Spring
(b)Summer
(c)Fall
(d)Winter
42°N
40°N
38°N
112°E
118°E
-40
-20
0
20
40
60
80
100
120
140
160
180
SH (Wm-2)

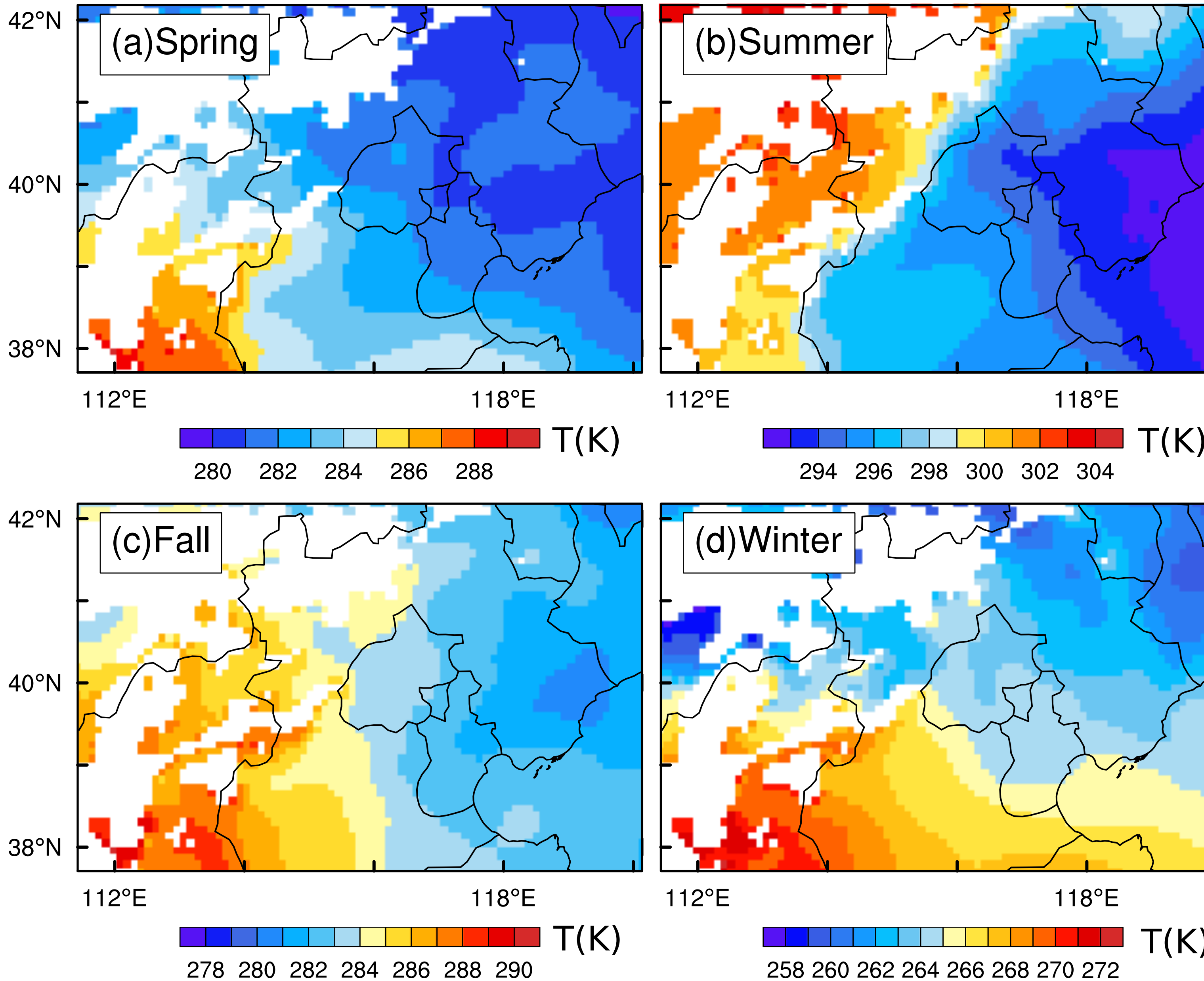
(a)Spring
(b)Summer
(c)Fall
(d)Winter
42°N
40°N
38°N
112°E
118°E
T(K)
280 282 284 286 288
294 296 298 300 302 304
278 280 282 284 286 288 290
258 260 262 264 266 268 270 272

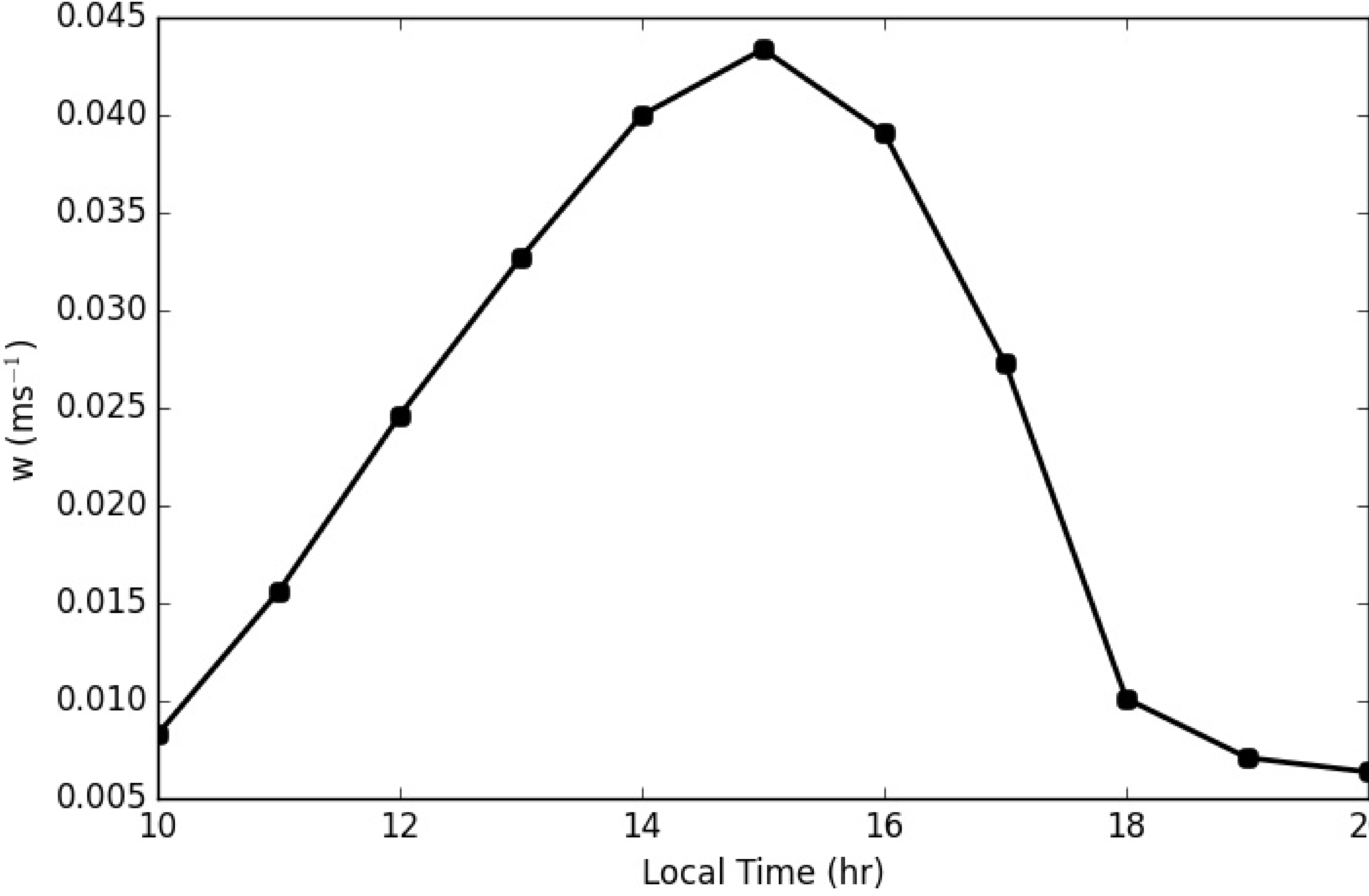

0.045
0.040
0.035
0.030
0.025
0.020
0.015
0.010
0.005
w (ms^{-1})
10
12
14
16
18
20
Local Time (hr)

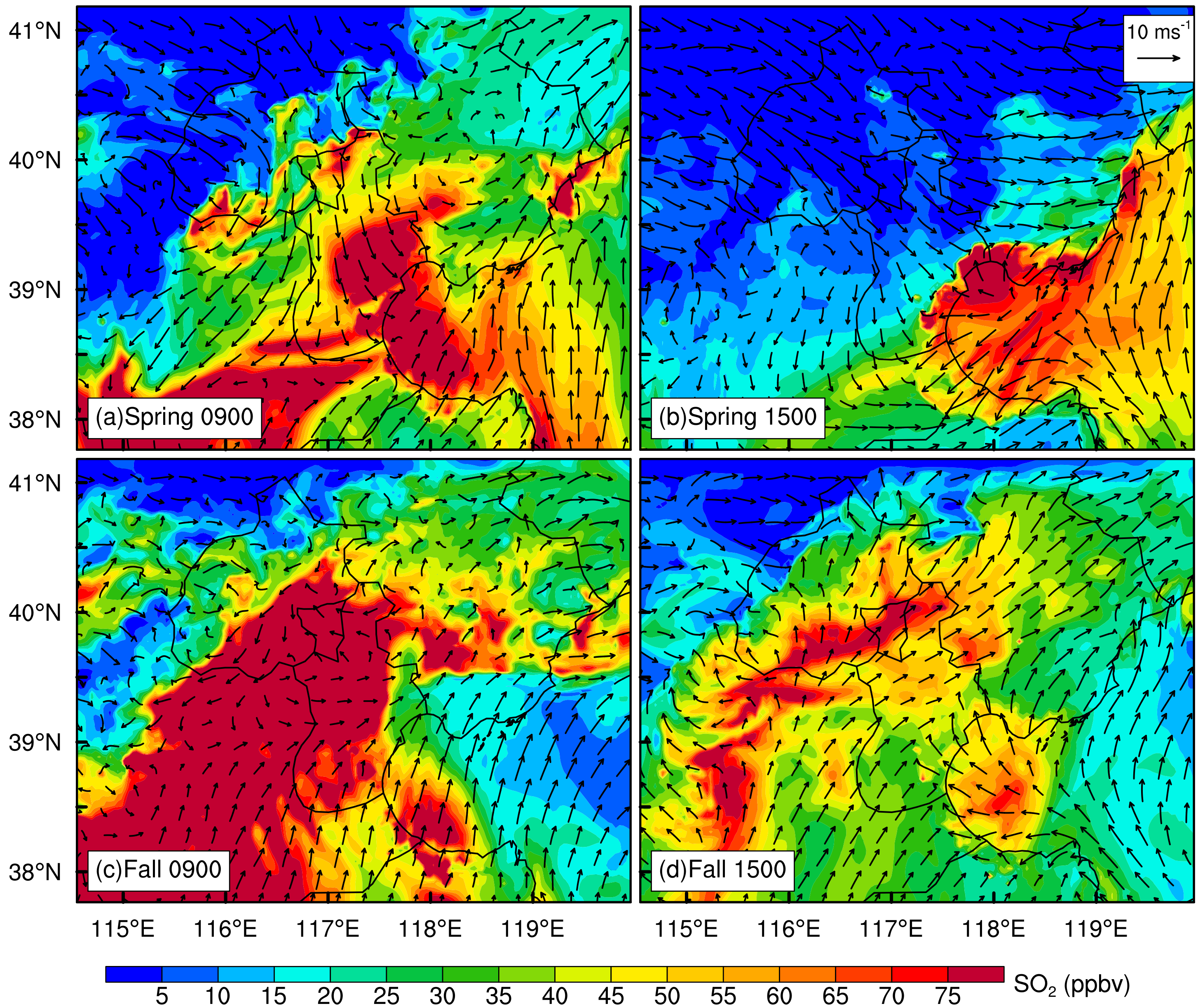
41°N
40°N
39°N
38°N
115°E
116°E
117°E
118°E
119°E
(a)Spring 0900
(b)Spring 1500
(c)Fall 0900
(d)Fall 1500
10 ms-1
5
10
15
20
25
30
35
40
45
50
55
60
65
70
75
SO2 (ppbv)

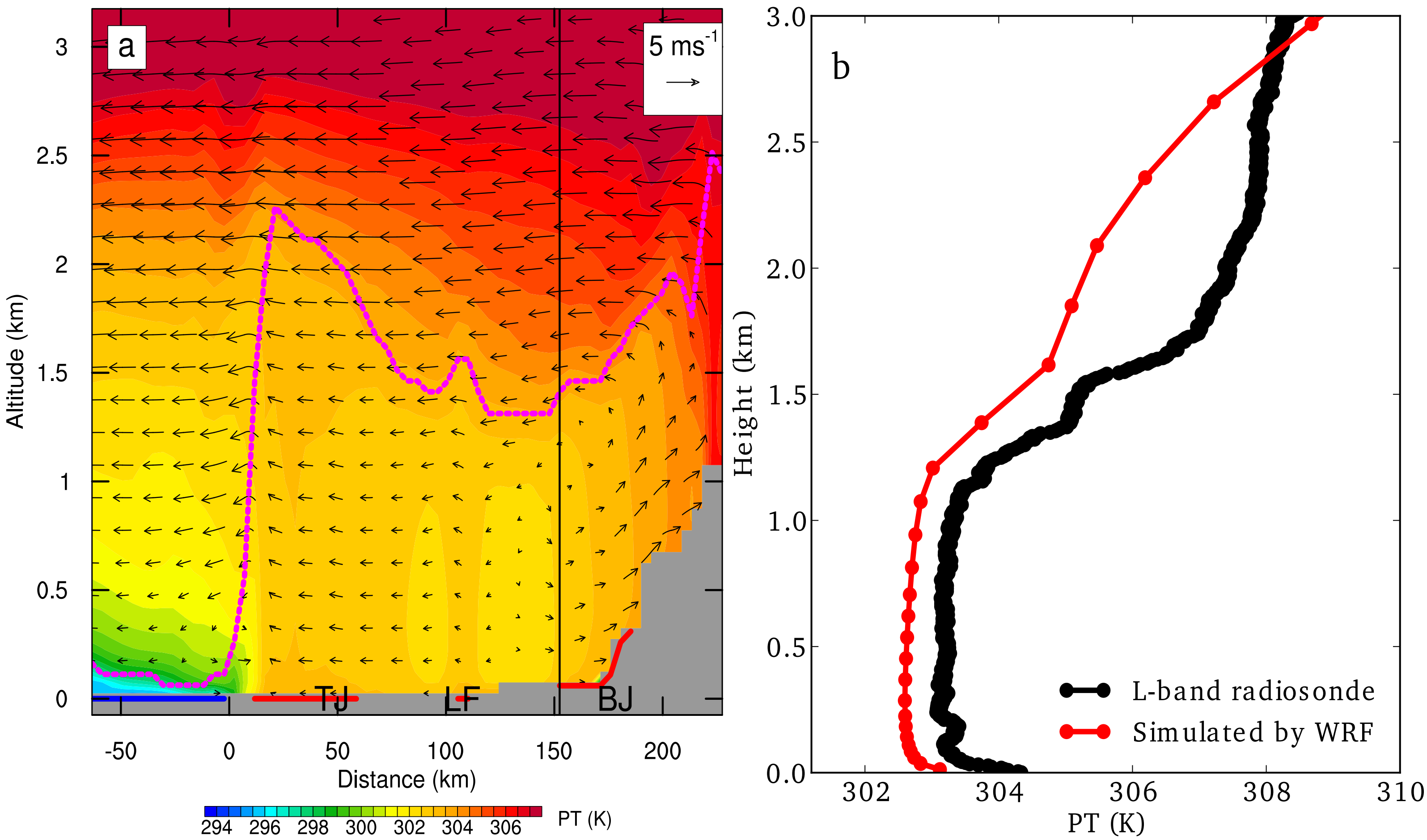
a
5 ms-1
Altitude (km)
Distance (km)
TJ
LF
BJ
294 296 298 300 302 304 306
PT (K)
b
Height (km)
PT (K)
L-band radiosonde
Simulated by WRF

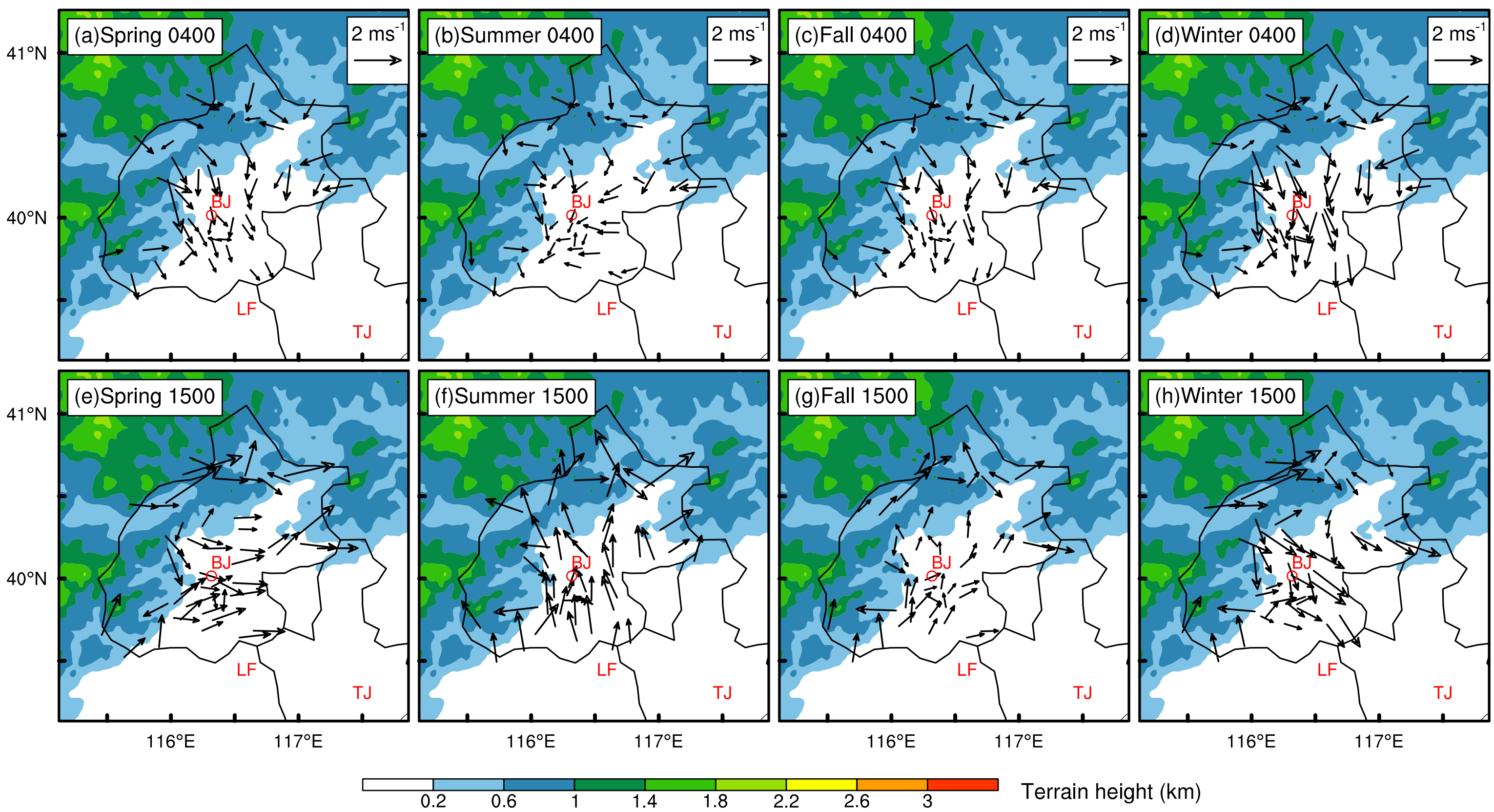

(a)Spring 0400
(b)Summer 0400
(c)Fall 0400
(d)Winter 0400
(e)Spring 1500
(f)Summer 1500
(g)Fall 1500
(h)Winter 1500
2 ms-1
BJ
LF
TJ
41°N
40°N
116°E
117°E
0.2
0.6
1
1.4
1.8
2.2
2.6
3
Terrain height (km)

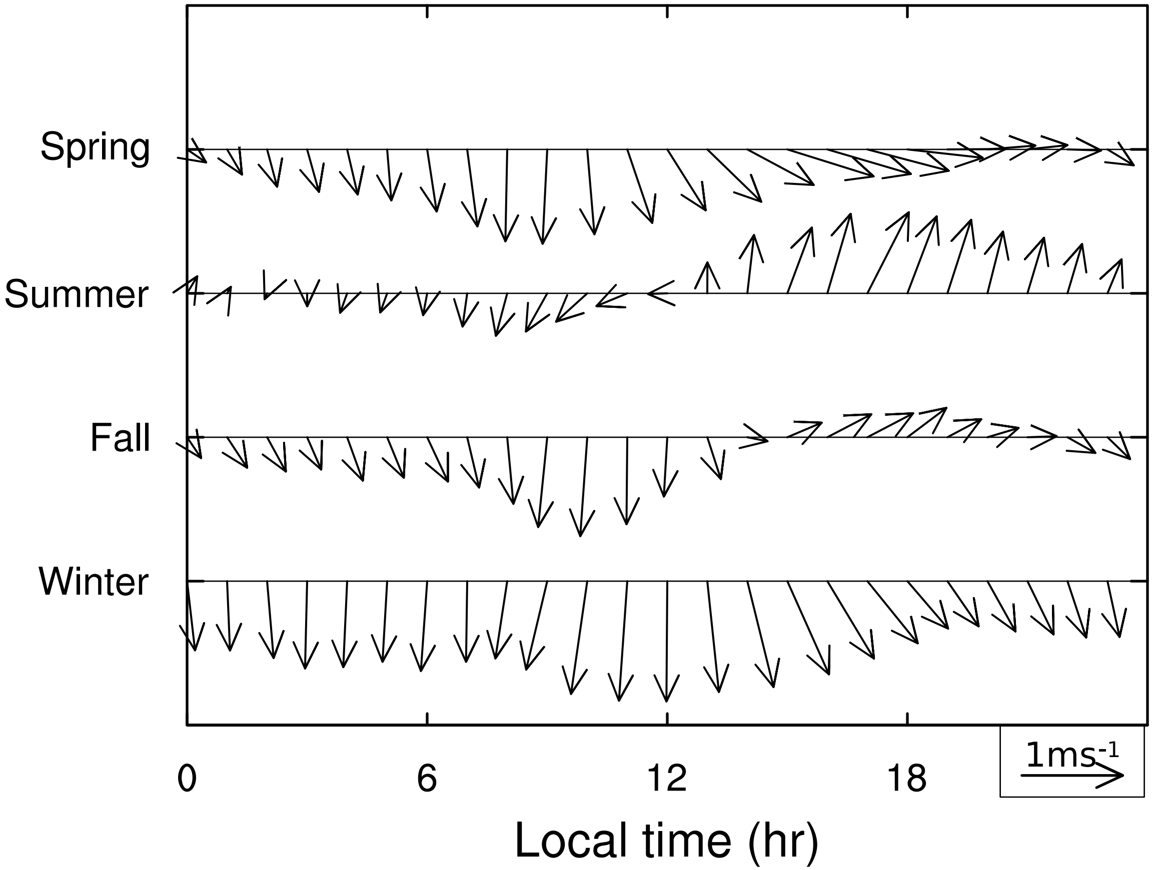

Spring
Summer
Fall
Winter
1ms-1
0
6
12
18
Local time (hr)

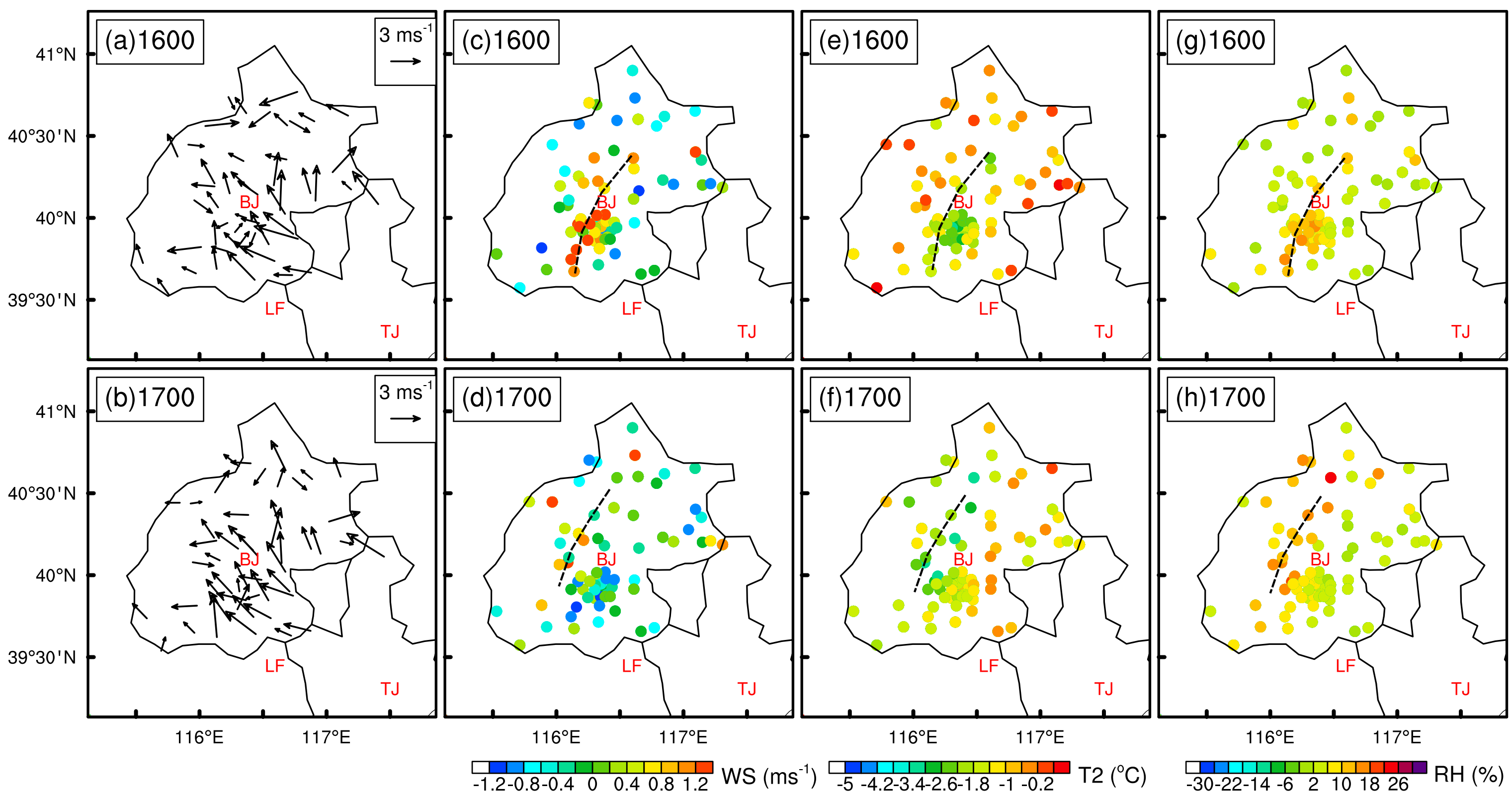

(a)1600
(b)1700
(c)1600
(d)1700
(e)1600
(f)1700
(g)1600
(h)1700
3 ms-1
BJ
LF
TJ
41°N
40°30'N
40°N
39°30'N
116°E
117°E
-1.2 -0.8 -0.4 0 0.4 0.8 1.2
WS (ms-1)
-5 -4.2 -3.4 -2.6 -1.8 -1 -0.2
T2 (°C)
-30 -22 -14 -6 2 10 18 26
RH (%)

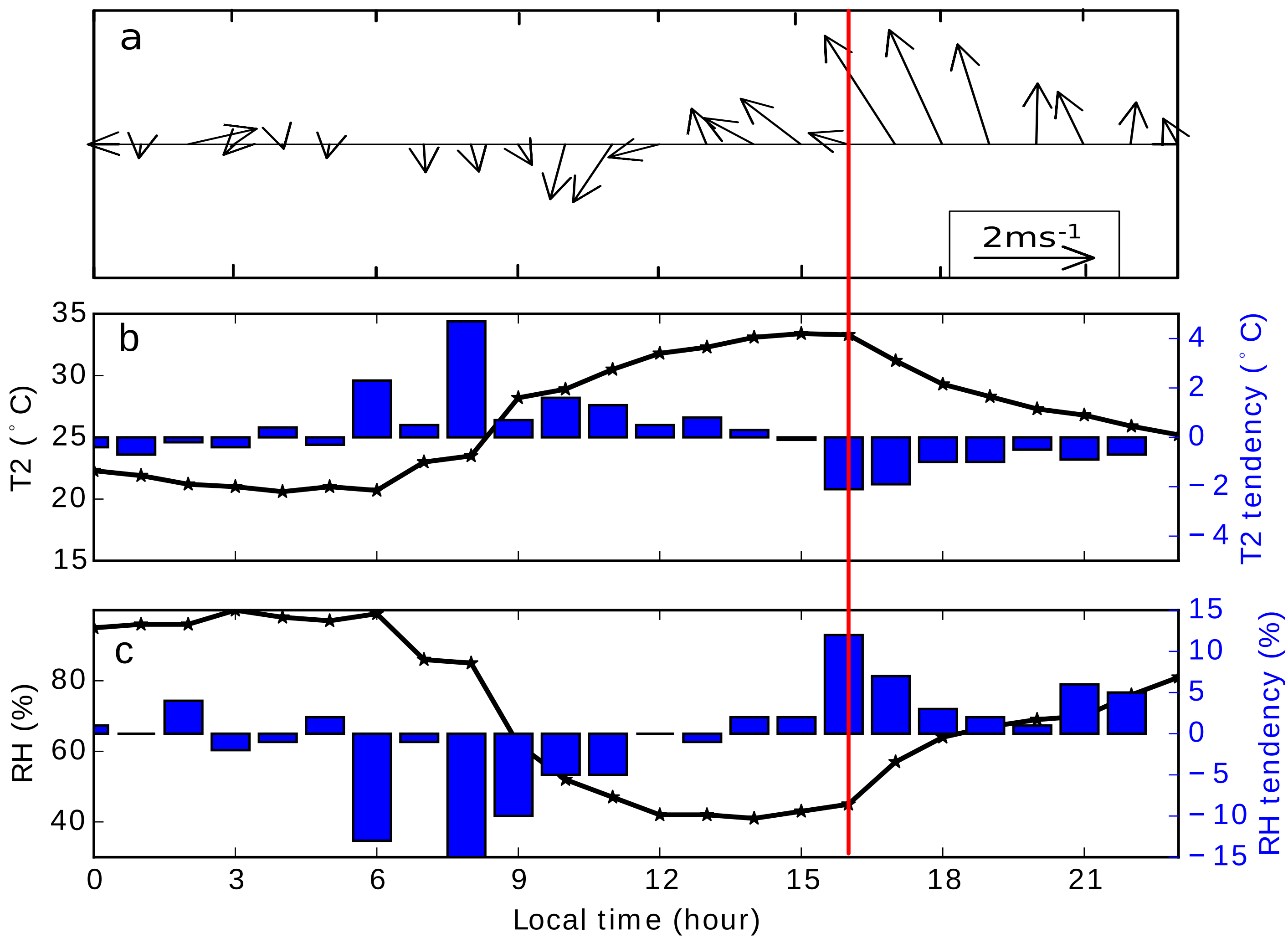

a
2ms-1
b
35
30
25
20
15
T2 (°C)
4
2
0
−2
−4
T2 tendency (°C)
c
80
60
40
RH (%)
15
10
5
0
−5
−10
−15
RH tendency (%)
0
3
6
9
12
15
18
21
Local time (hour)